Phys Chem Minerals (2002) 29: 369–385
DOI 10.1007/s00269-001-0236-0

ORIGINAL PAPER

R. T. Downs · G. V. Gibbs
M. B. Boisen Jr. · K. M. Rosso

A comparison of procrystal and ab initio model representations of the electron-density distributions of minerals

Received: 6 August 2001 / Accepted: 21 November 2001

Abstract The procrystal calculation of the electron density is a very rapid procedure that offers a quick way to analyze various bonding properties of a crystal. This study explores the extent to which the positions, number, and properties of bond-critical points determined from the procrystal representations of the electron density for minerals are similar to those of first-principles ab initio model distributions. The purpose of the study is to determine the limits imposed upon interpretation of the procrystal electron density. Procrystal calculations of the electron density for more than 300 *M*O bonds in crystals were compared with those previously calculated using CRYSTAL98 and TOPOND software. For every bond-critical point found in the ab initio calculations, an equivalent one was also found in the procrystal model, with similar magnitudes of electron density, and at similar positions along the bonds. The curvatures of the electron densities obtained from the ab initio and the procrystal distributions are highly correlated. It is concluded that the procrystal distributions are capable of providing good estimates of the bonded radii of the atoms and the properties of the electron-density distributions at the bond-critical points. Because the procrystal model is so fast to compute, it is especially useful in addressing the question as to whether a pair of atoms is bonded or not. If the Bader criteria for bonding are accepted, then the successful generation of the bond-critical points by the procrystal model demonstrates that bonding is an atomic feature. The main difference between the critical-point properties of the procrystal and the ab initio model is that the curvature in the electron density perpendicular to the bond path of the ab initio model is sharper than for the procrystal model. This is interpreted as indicating that the electrons that migrate into a bond originate from its sides, and not from the regions closer to the nuclei. This observation also suggests that ab initio optimization routines could see an improvement in speed if the parameters relating to the angular components of atomic wave functions were to vary before the radial components.

Keywords Electron density · Procrystal · Bond-critical points · Pyroxene · Feldspar · Topology

R. T. Downs (✉)
Department of Geosciences, University of Arizona,
Tucson, Arizona 85721, USA
Tel.: + 520-626-8092
Fax: + 520-621-2672
e-mail: downs@geo.arizona.edu

G. V. Gibbs
Department of Geological Sciences, Virginia Tech,
Blacksburg, Virginia 24061, USA

M. B. Boisen Jr
Department of Mathematics, University of Idaho,
Moscow, Idaho 83844-1103, USA

K. M. Rosso
W.R. Wiley Environmental Molecular Sciences Laboratory,
Pacific Northwest National Laboratory, PO Box 999,
KB-96, Richland, Washington 99352, USA

Introduction

The procrystal electron-density distribution of a crystal is constructed by superimposing spherically averaged electron-density distributions of static, ground state neutral atoms at the positions that the atoms occupy in the crystal. In practice, the atoms that contribute to the density at a given point are restricted to lie within a proscribed radius of that point, say within 5 Å. The calculations are quite rapid, requiring about 1 min for a modest-sized crystal on current PC technology. The difference between a procrystal electron-density distribution, $\rho(\mathbf{r})^{\mathrm{pro}}$, and that observed for a crystal, $\rho(\mathbf{r})$, is relatively small (Coppens 1997), and thus a close connection is also expected to exist between the properties of $\rho(\mathbf{r})$ and $\rho(\mathbf{r})^{\mathrm{pro}}$ (Spackman and Maslen 1985). Since the physical and chemical properties of a crystal are determined by its electron-density distribution, then it is likely that these properties may also be well determined by the procrystal distribution. For purposes of illustration, electron-density distributions (Fig. 1a, b) observed

for stishovite (Spackman et al. 1987) are compared with those calculated for the corresponding procrystal distributions (Fig. 1c, d). Both were evaluated for planes passing through the Si cation with Fig. 1a and c paralleling $(1\bar{1}1)$ and Fig. 1b and d paralleling (110). There is a greater localization of electron density displayed along the SiO bonds of the observed maps; however, the topography of the two distributions is quite similar.

Bond-critical point properties

In a series of ground-breaking papers on the nature of an electron-density distribution, Bader (1990) and his colleagues forged a powerful strategy for characterizing the distribution in terms of the properties at each of the stationary points (referred to as bond-critical points, bcp) that occur at local minima, $\mathbf{r}_C$, in the distribution along the bond path between each pair of bonded atoms, M and X. A bond path is a line, not necessarily straight, with the property that the electron density at each point along its length is a local maximum in the perpendicular plane (Bader 1998). With this definition, the bond-critical point properties of $\rho(\mathbf{r})$ and some of their attributes are described below.

1. $\rho(\mathbf{r}_C)$. The minimum value of the electron density along the bond path provides a measure of the strength of a given bond; the greater its value, the shorter the bond (Knop et al. 1988; Gibbs et al. 2001).

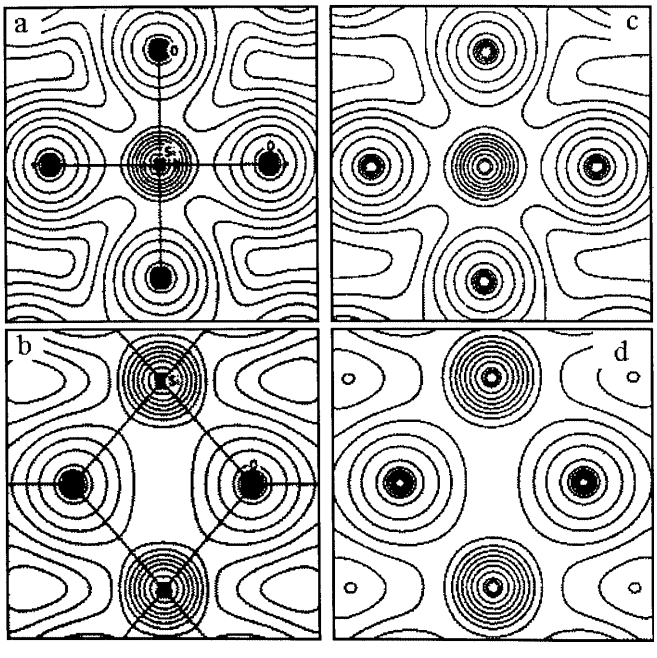

Fig. 1a–d Electron-density distributions (**a** and **b**) observed for stishovite (Spackman et al. 1987) are compared in **c** and **d** with those calculated for the corresponding procrystal distributions. Both were evaluated in the planes passing through the Si atom with **a** and **c** paralleling $(1\bar{1}1)$ and **b** and **d** paralleling (110). Despite the greater localization of the electron density displayed along the SiO bonds of the observed maps, the topography of the two distributions shows a close correspondence

2. $|\lambda_1|$, $|\lambda_2|$. The largest and smallest, respectively, of the curvatures of $\rho(\mathbf{r})$, measured at $\mathbf{r}_C$ in the plane perpendicular to the bond path. In general, the larger the values of $|\lambda_1|$ and $|\lambda_2|$, the sharper the maximum in $\rho(\mathbf{r})$ perpendicular to the path, and the greater the average localization of the electron density toward the path. The average value of these two curvatures is denoted $\lambda_{1,2} = (|\lambda_1| + |\lambda_2|)/2$. The ellipticity of a bond, defined as $\varepsilon = |\lambda_1|/|\lambda_2| - 1$, provides a measure of the anisotropy of $\rho(\mathbf{r})$ in a cross-section perpendicular to the bond path. A bond with an exceptionally large ε value is indicated to be susceptible to potential rupture (Bader 1990) and thus is a measure of the strength and stability of the bond.

3. λ_3: The curvature of $\rho(\mathbf{r})$ measured parallel to the path at $\mathbf{r}_C$. A larger value of λ_3 corresponds with a sharper minimum parallel to the bond path.

4. $\nabla^2\rho(\mathbf{r}_C)$. The Laplacian of the electron density at $\mathbf{r}_C$. It is a measure of the local concentration or depletion of $\rho(\mathbf{r})$ measured at $\mathbf{r}_C$. When $\nabla^2\rho(\mathbf{r}) < 0$, then $\rho(\mathbf{r})$ is said to be locally concentrated at $\mathbf{r}$; when $\nabla^2\rho(\mathbf{r}) > 0$, then $\rho(\mathbf{r})$ is said to be locally depleted at $\mathbf{r}$ (Bader 1990). Locally concentrated does not necessarily mean a large value of ρ, but rather, roughly, that the value of $\rho(\mathbf{r})$ is greater than the average value of the electron density in the immediate vicinity of $\mathbf{r}$. Bader (1990) also suggests that $\nabla^2\rho(\mathbf{r})$ is related to bond character, with large values corresponding to high degrees of ionicity.

5. $r_b(M)$, $r_b(X)$. The bonded radii of M and X are the distances between $\mathbf{r}_C$ and the positions of M and X, respectively, and so these radii describe the relative position of the bcp along the bond path between the pair of atoms.

An analysis of the total electron density at each point in a crystal would be time-consuming and would perhaps not provide a simple means for synthesis and understanding. However, the part of the density that is of greatest importance to crystal chemistry is that portion related to the interactions of pairs of atoms, the part involved in bonding. That is why ab initio methods using pseudopotentials, or a Gordon–Kim model that makes use of a Watson sphere (Cohen 1994), can be so successful; the models can afford to approximate nonbonded regions of the total electron density. The Bader (1990) approach suggests that it is sufficient to simply study the properties of the bond-critical points in order to understand the crystal chemistry of the entire crystal. For this reason, in this paper we analyze the similarities and differences between the procrystal and the ab initio model electron densities by comparing their bond-critical point properties.

Previous work

Procrystal and bonded radii

The distances between $\mathbf{r}_C$ and the positions of the atoms M and X in a procrystal representation of the electron-density distribution are defined to be the procrystal radii

of the two atoms, $r_b(M)^{pro}$ and $r_b(X)^{pro}$, respectively. A set of such radii has been determined for individual MX_6 octahedra obtained from the structures of 16 alkali-halide crystals (M = Li, Na, K, Rb; X = F, Cl, Br, I) (Gibbs et al. 1992). In their determination, the electron-density distributions of the atoms were spherically averaged and placed at the positions that they occupy in the rock salt structure to form a promolecule representation of the electron-density distribution of the octahedron. The bond paths of the octahedron were walked, the positions of the bcp along each path were found, and the promolecule radii of the atoms were determined. The resulting radii were found to agree within 0.03 Å, on average, with a set of ionic radii determined for the alkali halides by Tosi and Fumi (1964).

Promolecule radii have since been calculated for a large number of oxide-, nitride-, and sulfide-coordinated polyhedra with bond lengths clamped at the sums of effective ionic and crystal radii (Feth et al. 1993) derived by Shannon and Prewitt (1969), Shannon (1976, 1981), and Baur (1987). As observed for the Tosi–Fumi ionic radii, those calculated for both main-group and transition cations from the first four rows of the Periodic Table were found to be highly correlated with crystal and ionic radii derived for a large variety of crystalline materials. Remarkably, the radii calculated for the oxide, nitride, and sulfide anions correlate with the electronegativities of the cations to which they are "bonded". When "bonded" to highly electropositive cations, the anions were relatively large, approximating their ionic radii, but when "bonded" to highly electronegative cations, they were substantially smaller, approximating their atomic radii. The oxide anion, for example, adopted a radius of ~1.43 Å when bonded to K^+, a radius of 0.60 Å when bonded to N^{5+}, and a range of intermediate values between these two extremes that correlate with the electronegativities of the M cations (Feth et al. 1993). It was also found that promolecule radii calculated for the coordination polyhedra in several minerals match experimentally determined radii to within ~0.02 Å, on average (Feth et al. 1993), indicating that the position of $\mathbf{r}_C$ along the path is governed in large part by a procrystal component of the electron-density distribution and the separation between the bonded atoms; the redistribution of the electron density upon bond formation was concluded to play a minor role in governing the position of $\mathbf{r}_C$.

Given the close agreement between promolecule, crystal, and ionic radii, it would appear that a reliable estimate of the bonded radius of an atom in a crystal can be made by simply calculating the promolecule electron-density distribution for a representative coordination polyhedron (Gibbs et al. 1992; Feth et al. 1993). As argued earlier by Trefry et al. (1987), the close agreement between the promolecule and the Tosi–Fumi ionic radii suggests that the electron-density distribution of the alkali halides, particularly in the vicinity of $\mathbf{r}_C$, has a substantial component of procrystal character. They not only found that electron-density distributions calculated for several alkali crystals are strikingly similar to the distributions calculated for their procrystal representatives, but also that the electrostatic energies calculated for promolecule representatives provide closer estimates of the observed cohesive energies for the alkali halides, on average, than those obtained in lattice energy calculations. In addition to providing support for Slater's (1965) conclusion that the electron-density distributions of the alkali halides have a large component of atomic character, the strikingly similar distributions provide a basis for understanding why ionic and procrystal radii are similar.

Bond-critical point properties observed and calculated for the alkali halides and some molecular crystals

Tsirelson et al. (1998a, b) recently conducted a comparison of the critical-point properties determined from experimental, procrystal, and ab initio model (using CRYSTAL98) electron-density distributions for four cubic crystals (LiF, NaF, NaCl, MgO) with the rock salt structure. They found the number and positions of the bcps displayed by the three electron-density distributions to be similar. The values of the bcp properties experimentally observed for the four crystals are highly correlated with those calculated for their procrystal representatives. [$\rho(\mathbf{r})$ vs. $\rho(\mathbf{r})^{pro}$, $R^2 = 0.95$; $r_b(M)$ vs. $r_b(M)^{pro}$, $R^2 = 0.99$; $\lambda_{1,2}$ vs. $\lambda_{1,2}^{pro}$ $R^2 = 0.99$; λ_3 vs. λ_3^{pro}, $R^2 = 0.999$; $\nabla^2\rho(\mathbf{r})$ vs. $\nabla^2\rho(\mathbf{r})^{pro}$, $R^2 = 0.999$ where R^2 is the coefficient of determination]. However, in spite of the strong correlation, the experimental values recorded for $\lambda_{1,2}$, λ_3 and $\nabla^2\rho(\mathbf{r})$ depart by as much as 10% from those calculated for the procrystal representatives, while the experimental and procrystal values for $\rho(\mathbf{r})$ and $r_b(M)$ are virtually the same. The agreement between the experimental and the ab initio model calculations was found to be within 7%. Tsirelson et al. (1998a) remark that the correspondence of critical-point properties exhibited by the procrystal calculations forces them to question the Bader (1990) model that these critical points are necessary and sufficient conditions for bonding because "the procrystal is an unstable nonbonded system that does not obey the variational and Pauli exclusion principles and the virial theorem." However, Tsirelson et al. (1998a) also concluded that a mapping of the bcps for a procrystal representative is a reliable tool for estimating a priori the structural properties and features of crystals with the rock salt structure. Spackman and Maslen (1986) and Maslen and Etschmann (2000) reached similar conclusions in their studies of bonded interactions without ionization and chemical properties of diatomic molecules. Additionally, bcps from the procrystal have been found to match observed bcps for urea (Stewart 1991), L-alanine (Gatti et al. 1992), and solid molecular chlorine (Tsirelson et al. 1994).

Bond-critical point properties observed for silicate materials

Because of difficulties encountered in collecting a set of accurate single-crystal X-ray diffraction data (free from systematic errors), few efforts have been successful in accurately modeling the experimental electron-density distribution and obtaining a self-consistent set of bcp properties for a silicate. The efforts that have been undertaken include studies for bromellite (Downs 1991), danburite (Downs and Swope 1992), coesite (Downs 1995), topaz (Ivanov et al. 1998), scolecite (Kuntzinger et al. 1998), and several fibrous zeolites (Kirfel and Gibbs 2000). The properties obtained in these studies typically depart by as much as 10% or more from those calculated by ab initio quantum methods. Further, the trends reported between the experimental bcp properties and the bond lengths range between being well developed to being absent (Kirfel and Gibbs 2000). For example, in the case of topaz, the observed values of $\rho(\mathbf{r}_C)$ and R(SiO) were found to be highly correlated, shorter bond lengths involve larger $\rho(\mathbf{r})$ values, whereas, in the case of the zeolites, the correlations between $\rho(\mathbf{r}_C)$ and the SiO and AlO bond lengths were found to be weak or absent. For both coesite and danburite, correlations between R(SiO) and R(BO) vs. $\rho(\mathbf{r}_C)$ were found to be absent. In the case of the CaO bonds in danburite and the zeolites, however, a well-developed correlation obtains with shorter bonds involving larger $\rho(\mathbf{r}_C)$ values. In contrast, the NaO bond lengths for the zeolites were found to be independent of the value of $\rho(\mathbf{r}_C)$. For the bulk of these materials, the bond lengths were found to correlate with r_b(O) with smaller radii for the oxide anion tending to involve the shorter bonds. Meanwhile, several of the bcp properties were found to vary with bond length, as predicted by theory, but, for the most part, the correlations were either weak or absent. The absence and the inconsistency of the trends suggest that the observed electron-density distributions and bcp properties, at least in several cases, are affected, to one degree or another, by either incomplete datasets, or systematic error, or by both (Hill et al. 1983; Geisinger et al. 1987; Spackman et al. 1987; Downs 1995).

Bond-critical point properties calculated for model electron-density distributions

Given the lack of trends and the inconsistencies in the observed datasets, model electron-density distributions and bcp properties were calculated for the structures of a relatively large number of silicate and oxide materials (Gibbs et al. 2001). The aim of these calculations was to see whether the trends obtained between bond length and the bcp properties for the coordination polyhedra in hydroxyacid molecules containing first- and second-row M cations hold for those calculated for Earth materials (Hill et al. 1997; Gibbs et al. 2001). They were also undertaken to see how well the model distributions and their bcp properties agree with those observed (G.V. Gibbs, personal communication 2001). The materials for which model electron-density distributions, $\rho(\mathbf{r})^{mod}$, were calculated include the silica polymorphs quartz, coesite, cristobalite, and stishovite, the framework structures beryl, danburite, low albite, low microcline, the chain silicates tremolite, diopside, jadeite, and spodumene, the orthosilicates forsterite, topaz, and pyrope, and the oxides including calcite, magnesite, corundum, vanthoffite, anhydrite, berlinite, bromellite, and chrysoberyl (Gibbs et al. 2001). These materials were chosen for the study because they contain a variety of different MO-bonded interactions consisting of first- (Li, Be, B, C, N), second- (Na, Mg, Al, Si, P, S) and third-row (K, Ca) M cations. These MO bonds provide a relatively wide range of interactions ranging between closed-shell predominantly ionic and shared-electron covalent bonded interactions (Gibbs et al. 2001).

The wave functions and model electron-density distributions for these materials were calculated with CRYSTAL98 (Dovesi et al. 1996), an ab initio program that uses Gaussian orbital basis sets and periodic boundary conditions to calculate electronic wave functions at the Hartree–Fock or Kohn–Sham levels (Pisani 1996). The local density approximation was formulated using the Dirac–Slater exchange functional and the Vosko–Wilk–Nusair correlation functional. Electron basis sets developed and optimized specifically for use with CRYSTAL98 were used [e.g., a 65-111G* basis set for Si (D'Arco et al. 1993) and an 8-411G basis set for O (Dovesi et al. 1991)]. Observed cell parameters and atom coordinates along with the observed space group symmetries were used to generate the input structures. The bond-critical point properties of the electron-density distributions were calculated using TOPOND (Gatti 1997). Despite the wide range of bonded interactions, the resulting bcp properties were found to vary in a regular and consistent way with the observed bond lengths (Gibbs et al. 2001). In fact, the magnitudes of the bcp properties and the trends with bond length were found to be similar to those observed for the coordination polyhedra of the hydroxyacid molecules (Hill et al. 1997).

When plotted against the $\rho(\mathbf{r}_C)^{mod}$ values calculated for the silicate and oxide materials, the observed bond lengths, $R(M\text{O})$, were found to decrease monotonically with increasing value of $\rho(\mathbf{r}_C)^{mod}$, with the longer bond lengths decreasing at a higher rate for a given change in $\rho(\mathbf{r}_C)^{mod}$ than the shorter ones (Gibbs et al. 2001). In other words, a given increase in $\rho(\mathbf{r}_C)^{mod}$ is associated with a greater decrease in bond length for longer bonds like the NaO bonds than for shorter bonds like the SO bonds. Also, for a given bond length, bonded interactions involving second-row M cations generally display larger $\rho(\mathbf{r}_C)^{mod}$ values than the bonded inter-

actions involving first-row cations. For example, tetrahedral SiO and BeO bonds have about the same length, yet the $\rho(\mathbf{r}_C)^{mod}$ values for the SiO bond are about twice those of the BeO bond. Recall that the Pauling bond strength of the SiO bond is twice that of the BeO bond. This suggests, at least in this case, that the Pauling bond strength is a rough measure of $\rho(\mathbf{r}_C)^{mod}$, as observed by Gibbs et al. (2001). Accompanying the decrease in bond length, the magnitude of the curvatures of $\rho(\mathbf{r}_C)^{mod}$ perpendicular and parallel to the bond path both increase, demonstrating that the sharpness of the maximum of $\rho(\mathbf{r}_C)^{mod}$ perpendicular and the minimum parallel to the bond path both increase. Given that $\nabla^2\rho(\mathbf{r}_C)^{mod}$ tends to increase with decreasing bond length, the electron-density distribution at the bcp tends towards becoming depleted as $\rho(\mathbf{r}_C)$ increases in value. For each *M*O bond, the bonded radius of the oxide anion decreases linearly with decreasing *R*(*M*O). The r_b(O) values for first-row *M* cations are ~0.1 Å larger for a given bond length than those for second-row cations. Overall, the bonded radius of the oxide anion shows a wide range of values ranging from its ionic radius (~1.40 Å) when bonded to an electropositive cation like Na to its atomic radius (~0.65 Å) when bonded to an electronegative cation like N.

In as much as the difference between the model electron-density distributions calculated for the silicate and oxide materials and that calculated for procrystal representatives is expected to be small, a close connection is anticipated to exist between the properties of the two distributions, as observed by Tsirelson et al. (1998a, b) for the rock salt crystals. Also, if the trends found for the silicate and oxide materials hold for their procrystal representatives, then the determination of the bcp properties of a procrystal electron-density distribution can be used as a simple, yet powerful, tool for evaluating the bonded interactions in Earth materials, thereby providing a priori reliable estimates of their structural features and properties. In an earlier study, Downs et al. (1996) evaluated the bcp properties for the procrystal electron-density distributions of the feldspars low albite and low microcline and established a priori the bonded interactions and the coordination numbers for the Na and K cations. Also, an understanding of the bonded interactions that accompany the phase transitions between $P2_1/c$ and $C2/c$ in the pyroxenes clinoferrosilite and kanoite were obtained in a procrystal analysis (Downs et al. 1999). To further our understanding of the connection between properties of the procrystal electron-density distributions and those determined from ab initio models, procrystal representatives were constructed from the same silicate and oxide materials as studied by Gibbs et al. (2001) and the procrystal bcp properties were compared with those from the ab initio model distributions previously generated by Gibbs et al. (2001) for these materials. The goal of the study is to explore not only the extent to which the position and number of bcps portrayed by the procrystal representations are similar to those of model distributions, but also the extent to which the procrystal bcp properties correspond with the model bcp properties.

The data used for comparison

The bonding properties obtained from procrystal electron-density distributions are compared to distributions obtained from ab initio quantum calculations. It would be preferable to compare the procrystal distributions with experimentally observed data; however, as discussed above, there are not many experimental data, and their quality appears to be poorer than those obtained from quantum calculations.

Model distributions

Electron-density distributions, ρ^{mod}, and bcp properties were previously calculated for a relatively large number of silicate and oxide crystal structures, as listed above, by Gibbs et al. (2001) using the CRYSTAL98 (Dovesi et al. 1996) and TOPOND (Gatti 1997) software packages.

Procrystal distributions

The procrystal electron-density distribution for each of the crystals studied by Gibbs et al. (2001) was generated using the software SPEEDEN (SPhErical Electron DENsity) written for the PC (Downs et al. 1996). The bond-critical point properties for both the model and procrystal distributions are found in Table 1. The program reads the cell dimensions, space group, elemental atomic occupancies, and the positional parameters of the atoms in the asymmetric unit, and generates the contents of the cell. The procrystal electron density, $\rho(r)^{pro}$, at a point r in the crystal can then be computed with the expression (Gibbs et al. 1992)

$$\rho(\mathbf{r})^{pro} = 1/4\pi \sum_a \sum_t R_{a,t}[d_a(\mathbf{r})] \ ,$$

where *a* is an index to the atoms in the crystal structure, *t* is an index to each of the electrons associated with atom *a*, $R_{a,t}$ is the spherically averaged electron-density distribution generated for a wave function of type *t* for the atom defined by *a*, and $d_a(\mathbf{r})$ is the distance from the center of atom *a* to a point **r**. The electron density wavefunctions were obtained (Gibbs et al. 1992) by spherically averaging the electron-density distributions generated for the Roothaan–Hartree–Fock atomic wave functions tabulated by Clementi and Roetti (1974). The cell and atomic parameters are identical for both the model and procrystal calculations.

Table 1 Bond-critical point properties for 303 *M*O bonds, *M* = Al, Be, B, Ca, C, K, Li, Mg, Na, P, Si, and S for the ab initio model calculations and the procrystal calculations

$\rho^{mod}(\mathbf{r}_C)$	$\nabla^2\rho(\mathbf{r}_C)^{mod}$	λ_1^{mod}	λ_2^{mod}	λ_3^{mod}	$r_b(O)^{mod}$	R(*M*O)	$\rho^{pro}(\mathbf{r}_C)$	$\nabla^2\rho(\mathbf{r}_C)^{pro}$	λ_1^{pro}	λ_2^{pro}	λ_3^{pro}	$r_b(O)^{pro}$	Bond
0.4950	10.92	−2.89	−2.82	16.62	1.073	1.852	0.4517	9.14	−1.87	−1.81	12.81	1.048	AlO_1
0.4886	10.59	−2.95	−2.75	16.29	1.084	1.865	0.4401	8.71	−1.79	−1.74	12.24	1.057	AlO_5
0.4702	10.20	−2.66	−2.61	15.47	1.087	1.873	0.4368	8.38	−1.64	−1.71	11.74	1.062	AlO_4
0.4252	8.92	−2.35	−2.26	13.52	1.112	1.910	0.4049	7.10	−1.48	−1.43	10.02	1.085	AlO_2
0.4028	8.28	−2.10	−2.05	12.43	1.128	1.934	0.3941	6.44	−1.34	−1.28	9.05	1.100	AlO_4
0.3565	6.91	−1.76	−1.67	10.35	1.163	1.985	0.3629	5.09	−1.13	−1.02	7.23	1.131	AlO_1
0.5109	11.65	−2.96	−2.92	17.53	1.065	1.827	0.4799	10.14	−1.96	−2.07	14.17	1.033	$Al1O_1$
0.2847	4.84	−1.17	−1.17	7.18	1.232	2.086	0.3128	3.03	−0.78	−0.72	4.54	1.188	$Al1O_4$
0.4521	9.47	−2.51	−2.46	14.44	1.100	1.898	0.4164	7.51	−1.43	−1.57	10.52	1.078	$Al2O_3$
0.5415	12.46	−3.32	−3.19	18.97	1.047	1.814	0.4812	10.61	−2.14	−2.19	14.93	1.023	$Al2O_4$
0.5109	11.65	−2.96	−2.92	17.53	1.065	1.839	0.4640	9.65	−1.83	−2.01	13.48	1.041	$Al2O_3$
0.4521	9.47	−2.51	−2.46	14.44	1.100	1.892	0.4229	7.74	−1.52	−1.61	10.87	1.074	$Al1O_2$
0.4461	9.60	−2.47	−2.41	14.47	1.097	1.889	0.4226	7.78	−1.58	−1.57	10.93	1.072	AlO
0.3751	7.67	−1.94	−1.88	11.49	1.141	1.954	0.3771	5.80	−1.25	−1.20	8.25	1.112	$Al1O_4$
0.4926	10.19	−2.73	−2.68	15.60	1.086	1.868	0.4403	8.51	−1.74	−1.68	11.94	1.059	$Al1O_2$
0.4227	8.83	−2.25	−2.23	13.31	1.114	1.913	0.4070	7.02	−1.46	−1.38	9.87	1.088	$Al1O_1$
0.6895	18.13	−4.42	−4.40	26.95	0.975	1.711	0.5980	15.88	−3.31	−3.30	22.49	0.954	$Al2O_3$
0.6554	15.66	−4.06	−3.95	23.67	1.006	1.751	0.5492	13.61	−2.82	−2.78	19.20	0.982	$Al2O_2$
0.5706	13.35	−3.58	−3.43	20.36	1.036	1.796	0.5025	11.45	−2.30	−2.35	16.10	1.012	$Al2O_4$
0.4560	9.63	−2.54	−2.50	14.66	1.098	1.888	0.4240	7.85	−1.62	−1.55	11.02	1.071	AlO_3
0.4443	9.26	−2.43	−2.40	14.09	1.105	1.898	0.4174	7.50	−1.56	−1.48	10.54	1.078	AlO_3
0.4476	9.36	−2.47	−2.41	14.24	1.103	1.895	0.4193	7.61	−1.57	−1.51	10.69	1.076	AlO_1
0.4439	9.24	−2.43	−2.38	14.05	1.105	1.899	0.4163	7.48	−1.47	−1.56	10.51	1.079	AlO_2
0.4096	8.19	−2.17	−2.11	12.47	1.129	1.933	0.3935	6.43	−1.30	−1.36	9.09	1.100	AlO_1
0.3487	6.58	−1.69	−1.66	9.93	1.171	1.996	0.3562	4.79	−1.06	−1.01	6.87	1.138	AlO_1
0.4832	10.60	−2.74	−2.70	16.04	1.074	1.856	0.4444	8.87	−1.82	−1.81	12.50	1.050	AlO_2
0.5282	12.11	−3.11	−3.07	18.29	1.050	1.820	0.4774	10.31	−2.10	−2.09	14.50	1.027	$Al1O_2$
0.3984	7.92	−2.07	−2.03	12.02	1.136	1.943	0.3882	6.14	−1.25	−1.30	8.69	1.107	$Al1O_1$
0.3464	6.55	−1.68	−1.64	9.86	1.173	1.999	0.3567	4.75	−1.04	−1.01	6.80	1.140	$Al1O_1$
0.4278	9.04	−2.31	−2.30	13.64	1.109	1.906	0.4102	7.24	−1.42	−1.52	10.17	1.084	AlO_2
0.6696	16.94	−4.30	−4.18	25.41	0.990	1.730	0.5727	14.75	−3.04	−3.06	20.85	0.968	AlO(C)o
0.6469	16.36	−4.13	−4.07	24.57	0.995	1.739	0.5622	14.24	−2.95	−2.93	20.12	0.974	AlO(B)o
0.6522	16.4	−4.15	−4.07	24.61	0.996	1.740	0.5626	14.23	−2.95	−2.92	20.10	0.974	AlO(D)o
0.6396	16.13	−4.08	−4.01	24.22	0.998	1.743	0.5583	14.01	−2.89	−2.89	19.79	0.977	AlO(A1)
0.6899	18.08	−4.49	−4.42	26.99	0.978	1.713	0.5966	15.74	−3.28	−3.27	22.29	0.956	Al1oOdo
0.6732	17.60	−4.35	−4.34	26.29	0.981	1.719	0.5869	15.36	−3.20	−3.19	21.75	0.960	Al1oObo
0.6404	15.92	−4.08	−3.96	23.96	1.002	1.747	0.5516	13.80	−2.84	−2.86	19.50	0.979	Al1oOco
0.6135	15.19	−3.87	−3.79	22.85	1.009	1.760	0.5375	13.13	−2.71	−2.70	18.54	0.987	Al1oOa1
0.6435	16.85	−4.23	−4.13	25.21	0.990	1.732	0.5653	14.61	−3.03	−3.02	20.66	0.969	AlO_1
0.6224	16.10	−4.02	−3.97	24.09	0.999	1.745	0.5489	13.88	−2.88	−2.86	19.62	0.978	AlO_2
0.5009	10.74	−2.84	−2.80	16.37	1.077	1.856	0.4561	8.97	−1.77	−1.83	12.57	1.051	AlO
0.3891	7.41	−1.84	−1.79	11.04	1.155	1.969	0.3886	5.57	−1.15	−1.07	7.79	1.123	AlO
0.4625	9.62	−2.43	−2.41	14.47	1.102	1.893	0.4387	7.80	−1.50	−1.54	10.83	1.076	$Al1O_2$
0.4951	10.68	−2.73	−2.71	16.13	1.082	1.862	0.4606	8.84	−1.75	−1.70	12.30	1.056	$Al1O_1$
0.4497	8.94	−2.32	−2.29	13.55	1.115	1.911	0.4239	7.19	−1.44	−1.38	10.01	1.087	$Al1O_3$
0.4818	10.42	−2.73	−2.72	15.88	1.081	1.864	0.4430	8.64	−1.76	−1.76	12.16	1.056	$Al2O_2$
0.4545	9.35	−2.49	−2.47	14.30	1.102	1.894	0.4195	7.60	−1.55	−1.57	10.72	1.075	$Al2O_3$
0.4038	8.12	−2.04	−2.04	12.21	1.135	1.941	0.3994	6.31	−1.25	−1.28	8.85	1.107	$Al2O_1$
0.3425	6.14	−1.54	−1.52	9.20	1.189	2.020	0.3562	4.36	−0.94	−0.90	6.20	1.155	$Al2O_3$
0.5483	12.07	−4.28	−4.09	20.45	1.041	1.612	0.4171	13.33	−2.30	−2.35	17.97	1.044	BeO_5
0.5109	11.17	−3.80	−3.66	18.64	1.054	1.632	0.4009	12.29	−2.12	−2.09	16.49	1.058	BeO_2
0.4719	10.28	−3.38	−3.28	16.94	1.070	1.657	0.3799	11.13	−1.86	−1.91	14.90	1.076	BeO_3
0.4610	9.91	−3.29	−3.16	16.36	1.078	1.667	0.3727	10.69	−1.79	−1.82	14.30	1.084	BeO_3
0.4895	11.07	−3.54	−3.42	18.03	1.064	1.638	0.3953	11.98	−2.04	−2.06	16.08	1.063	$Be1O_2$
0.4832	11.00	−3.47	−3.40	17.87	1.065	1.640	0.3930	11.88	−2.05	−2.01	15.94	1.064	$Be1O_4$
0.4803	10.90	−3.48	−3.36	17.73	1.067	1.643	0.3915	11.78	−2.03	−2.00	15.82	1.066	$Be1O_1$
0.4657	10.35	−3.29	−3.19	16.83	1.077	1.657	0.3816	11.17	−1.91	−1.87	14.95	1.077	$Be1O_4$
0.4976	11.36	−3.67	−3.56	18.59	1.058	1.630	0.4011	12.38	−2.15	−2.12	16.65	1.057	$Be2O_1$
0.4905	11.08	−3.55	−3.42	18.05	1.064	1.638	0.3954	11.99	−2.05	−2.06	16.10	1.063	$Be2O_2$
0.4666	10.35	−3.29	−3.22	16.87	1.076	1.656	0.3814	11.16	−1.90	−1.87	14.93	1.076	$Be2O_3$
0.4633	10.46	−3.23	−3.15	16.85	1.076	1.656	0.3816	11.19	−1.92	−1.88	14.99	1.076	$Be2O_3$
0.4781	10.22	−3.45	−3.27	16.93	1.070	1.656	0.3846	11.22	−1.97	−1.79	14.97	1.076	BeO_2
0.5936	13.39	−4.66	−4.59	22.64	1.018	1.581	0.4529	14.90	−2.68	−2.67	20.25	1.021	BeO_1
0.5208	10.86	−3.60	−3.53	17.99	1.060	1.641	0.4143	11.98	−1.96	−1.99	15.93	1.065	BeO_3
0.4516	9.36	−2.78	−2.77	14.92	1.098	1.693	0.3817	9.79	−1.51	−1.53	12.84	1.105	BeO_2
0.4981	10.80	−3.49	−3.49	17.78	1.064	1.646	0.4014	11.73	−1.97	−1.96	15.67	1.069	BeO
0.4856	10.47	−3.33	−3.33	17.12	1.071	1.656	0.3942	11.28	−1.88	−1.88	15.04	1.077	BeO

Table 1 (Contd.)

$\rho^{mod}(\mathbf{r}_C)$	$\nabla^2\rho(\mathbf{r}_C)^{mod}$	λ_1^{mod}	λ_2^{mod}	λ_3^{mod}	$r_b(O)^{mod}$	R(*MO*)	$\rho^{pro}(\mathbf{r}_C)$	$\nabla^2\rho(\mathbf{r}_C)^{pro}$	λ_1^{pro}	λ_2^{pro}	λ_3^{pro}	$r_b(O)^{pro}$	Bond
0.9921	7.41	−7.55	−7.34	22.30	1.004	1.500	0.8636	9.63	−3.19	−3.13	15.95	0.994	BO
1.129	8.56	−9.41	−9.21	27.18	0.971	1.454	0.9131	14.25	−3.88	−3.93	22.07	0.964	BO
1.076	9.39	−8.70	−8.57	26.67	0.978	1.463	0.9030	13.32	−3.72	−3.78	20.83	0.970	BO
1.030	8.63	−8.11	−8.01	24.74	0.989	1.479	0.8838	11.64	−3.51	−3.46	18.62	0.980	BO
1.473	18.70	−14.48	−14.13	47.31	0.885	1.337	1.0998	30.01	−6.68	−6.90	43.60	0.879	$B1O_3$
1.393	15.02	−13.04	−12.94	40.99	0.906	1.366	1.0425	25.50	−5.81	−6.04	37.35	0.901	$B1O_2$
1.260	11.90	−11.43	−11.13	34.45	0.934	1.404	0.9792	20.16	−5.07	−4.77	30.00	0.929	$B1O_1$
1.323	14.37	−12.32	−11.98	38.67	0.917	1.380	1.0178	23.46	−5.42	−5.65	34.53	0.911	$B2O_3$
1.488	18.20	−14.47	−14.27	46.93	0.886	1.337	1.0965	29.86	−6.67	−6.88	43.41	0.880	$B2O_1$
1.273	11.63	−11.49	−11.32	34.44	0.933	1.403	0.9798	20.32	−5.10	−4.82	30.24	0.928	$B2O_2$
0.2970	4.56	−1.27	−1.23	7.06	1.168	2.322	0.2515	4.73	−0.86	−0.96	6.55	1.137	$Ca4O_4$
0.2442	3.80	−1.01	−0.97	5.78	1.199	2.396	0.2124	3.83	−0.71	−0.72	5.26	1.177	$Ca4O_2$
0.1724	2.67	−0.65	−0.59	3.91	1.279	2.541	0.1652	2.65	−0.48	−0.33	3.45	1.266	$Ca4O_6$
0.1004	1.53	−0.34	−0.30	2.18	1.409	2.767	0.1089	1.37	−0.12	−0.23	1.73	1.398	$Ca4O_5$
0.2759	4.19	−1.15	−1.12	6.46	1.181	2.353	0.2353	4.34	−0.77	−0.86	5.98	1.154	CaO_6
0.2650	4.17	−1.12	−1.08	6.37	1.182	2.360	0.2299	4.24	−0.80	−0.82	5.86	1.157	CaO_6
0.1661	2.55	−0.61	−0.56	3.72	1.292	2.561	0.1605	2.50	−0.44	−0.31	3.25	1.278	CaO_6
0.1138	1.74	−0.39	−0.37	2.50	1.381	2.717	0.1182	1.58	−0.26	−0.19	2.03	1.364	CaO_6
0.2402	3.74	−1.05	−0.98	5.78	1.203	2.401	0.2010	3.76	−0.69	−0.73	5.19	1.179	CaO
0.2024	3.30	−0.84	−0.80	4.94	1.229	2.455	0.1809	3.26	−0.55	−0.62	4.42	1.211	CaO
0.2013	3.17	−0.85	−0.79	4.81	1.239	2.467	0.1760	3.14	−0.55	−0.58	4.27	1.218	CaO
0.1824	2.94	−0.72	−0.69	4.35	1.257	2.500	0.1655	2.88	−0.54	−0.45	3.87	1.237	CaO
0.2389	4.37	−1.02	−1.01	6.40	1.189	2.342	0.2240	4.36	−0.89	−0.87	6.12	1.144	CaO_2
0.1788	2.84	−0.69	−0.69	4.22	1.261	2.509	0.1664	2.85	−0.52	−0.40	3.78	1.245	CaO_2
0.1591	2.46	−0.60	−0.60	3.66	1.291	2.564	0.1457	2.42	−0.33	−0.44	3.20	1.276	CaO_1
0.1915	3.19	−0.80	−0.78	4.77	1.231	2.461	0.1726	3.14	−0.60	−0.58	4.32	1.211	CaO_1
0.2320	3.48	−0.91	−0.90	5.30	1.215	2.425	0.2040	3.57	−0.57	−0.68	4.82	1.198	CaO_3
0.2103	3.12	−0.84	−0.80	4.77	1.237	2.461	0.1793	3.15	−0.59	−0.57	4.32	1.212	CaO_2
0.1995	3.14	−0.79	−0.77	4.70	1.243	2.476	0.1855	3.13	−0.50	−0.58	4.20	1.226	CaO_1
0.1263	1.82	−0.43	−0.41	2.66	1.374	2.693	0.1252	1.69	−0.18	−0.29	2.15	1.356	CaO_3
0.1218	1.69	−0.42	−0.40	2.52	1.388	2.713	0.1147	1.54	−0.26	−0.24	2.04	1.354	CaO_2
0.2556	4.18	−1.15	−1.08	6.41	1.187	2.357	0.2202	4.21	−0.82	−0.84	5.87	1.154	CaO
2.375	−14.5	−20.69	−19.63	25.79	0.826	1.283	1.9768	−2.27	−9.80	−10.12	17.65	0.808	CO
2.357	−14.6	−20.20	−19.28	24.87	0.827	1.286	1.9703	−2.54	−9.76	−10.08	17.29	0.808	CO
0.1098	1.73	−0.37	−0.36	2.45	1.397	2.762	0.1017	1.68	−0.25	−0.31	2.24	1.337	KOa_2
0.0952	1.43	−0.30	−0.29	2.02	1.428	2.846	0.0876	1.36	−0.24	−0.19	1.79	1.382	KOa_1
0.0931	1.40	−0.29	−0.28	1.98	1.432	2.855	0.0868	1.34	−0.23	−0.18	1.75	1.387	KOa_1
0.0853	1.29	−0.26	−0.25	1.80	1.450	2.891	0.0788	1.21	−0.13	−0.21	1.55	1.414	KOco
0.0795	1.18	−0.24	−0.24	1.67	1.465	2.926	0.0730	1.10	−0.19	−0.14	1.43	1.425	KOdo
0.0721	1.06	−0.21	−0.21	1.48	1.489	2.975	0.0692	1.00	−0.17	−0.11	1.27	1.455	KObo
0.1367	3.19	−0.71	−0.69	4.58	1.320	2.107	0.1157	2.83	−0.44	−0.43	3.70	1.305	$Li2O_1$
0.0901	2.02	−0.45	−0.36	2.83	1.412	2.253	0.0879	1.84	−0.28	−0.17	2.30	1.413	$Li2O_3$
0.0913	1.95	−0.41	−0.32	2.67	1.435	2.279	0.0890	1.77	−0.15	−0.26	2.18	1.428	$Li2O_2$
0.2029	4.34	−1.00	−1.00	6.34	1.252	2.000	0.1809	3.86	−0.70	−0.70	5.26	1.226	LiO
0.2681	6.32	−1.25	−1.23	8.79	1.174	2.068	0.2694	5.38	−0.88	−0.98	7.24	1.153	$Mg1O_2$
0.2502	5.95	−1.16	−1.16	8.27	1.182	2.084	0.2526	4.98	−0.93	−0.88	6.79	1.159	$Mg1O_1$
0.2331	5.18	−1.01	−0.98	7.18	1.216	2.130	0.2409	4.32	−0.64	−0.79	5.74	1.194	$Mg1O_3$
0.2665	6.60	−1.36	−1.30	9.26	1.159	2.049	0.2616	5.59	−1.05	−1.05	7.69	1.136	$Mg2O_2$
0.2562	6.22	−1.28	−1.23	8.73	1.171	2.067	0.2513	5.24	−0.98	−0.99	7.21	1.147	$Mg2O_3$
0.1972	4.40	−0.86	−0.85	6.11	1.246	2.180	0.2099	3.53	−0.65	−0.61	4.78	1.219	$Mg2O_1$
0.1883	3.99	−0.78	−0.75	5.53	1.271	2.213	0.2060	3.19	−0.46	−0.58	4.23	1.247	$Mg2O_3$
0.1977	4.20	−0.85	−0.81	5.85	1.260	2.197	0.2101	3.41	−0.52	−0.62	4.55	1.233	MgO
0.1353	2.66	−0.50	−0.45	3.62	1.359	2.349	0.1622	1.86	−0.35	−0.30	2.52	1.319	MgO
0.2567	6.34	−1.26	−1.22	8.81	1.169	2.065	0.2614	5.34	−0.98	−0.98	7.31	1.147	$Mg1O_1$
0.2497	6.05	−1.21	−1.17	8.43	1.178	2.078	0.2536	5.07	−0.93	−0.94	6.94	1.155	$Mg1O_2$
0.2522	6.05	−1.24	−1.17	8.46	1.184	2.083	0.2471	4.93	−0.91	−0.90	6.74	1.156	$Mg1O_3$
0.2841	7.35	−1.44	−1.41	10.20	1.133	2.014	0.2849	6.29	−1.21	−1.19	8.69	1.113	$Mg2O_4$
0.2463	5.95	−1.19	−1.15	8.28	1.182	2.084	0.2519	4.96	−0.92	−0.91	6.79	1.159	$Mg2O_2$
0.2167	5.11	−1.00	−0.97	7.08	1.214	2.133	0.2300	4.18	−0.75	−0.75	5.68	1.190	$Mg2O_1$
0.2713	6.56	−1.37	−1.28	9.21	1.168	2.058	0.2597	5.38	−0.99	−1.00	7.38	1.141	$Mg3O_3$
0.2549	6.23	−1.24	−1.20	8.67	1.173	2.070	0.2580	5.24	−0.96	−0.96	7.15	1.150	$Mg3O_1$
0.2590	6.52	−1.27	−1.24	9.03	1.157	2.050	0.2645	5.53	−1.05	−1.03	7.62	1.136	MgO_6
0.2564	6.31	−1.26	−1.22	8.79	1.169	2.065	0.2619	5.31	−0.99	−0.97	7.28	1.147	MgO_6
0.2259	5.38	−1.06	−1.03	7.47	1.202	2.115	0.2377	4.45	−0.82	−0.80	6.07	1.178	MgO_6
0.2752	6.74	−1.33	−1.30	9.37	1.158	2.046	0.2756	5.69	−1.03	−1.05	7.77	1.135	$Mg1O_4$
0.2330	5.40	−1.05	−1.03	7.47	1.203	2.115	0.2412	4.44	−0.78	−0.80	6.03	1.178	$Mg1O_3$
0.3004	7.07	−1.38	−1.37	9.82	1.155	2.035	0.2873	5.95	−1.07	−1.09	8.12	1.129	$Mg2O_1$
0.2450	5.80	−1.14	−1.11	8.04	1.189	2.093	0.2505	4.82	−0.86	−0.88	6.56	1.165	$Mg2O_4$

Table 1 (Contd.)

$\rho^{mod}(\mathbf{r}_C)$	$\nabla^2\rho(\mathbf{r}_C)^{mod}$	λ_1^{mod}	λ_2^{mod}	λ_3^{mod}	$r_b(O)^{mod}$	R(*MO*)	$\rho^{pro}(\mathbf{r}_C)$	$\nabla^2\rho(\mathbf{r}_C)^{pro}$	λ_1^{pro}	λ_2^{pro}	λ_3^{pro}	$r_b(O)^{pro}$	Bond
0.2346	5.72	−1.18	−1.12	8.02	1.188	2.095	0.2402	4.76	−0.86	−0.90	6.52	1.165	$Mg2O_2$
0.3071	7.46	−1.46	−1.41	10.33	1.140	2.016	0.2977	6.33	−1.14	−1.20	8.67	1.116	$Mg3O_1$
0.2295	5.27	−1.03	−1.01	7.31	1.209	2.123	0.2386	4.32	−0.76	−0.78	5.86	1.184	$Mg3O_3$
0.2244	5.21	−1.01	−0.98	7.20	1.212	2.128	0.2369	4.26	−0.77	−0.74	5.77	1.186	$Mg3O_4$
0.2417	6.24	−1.25	−1.20	8.69	1.160	2.058	0.2512	5.35	−1.02	−1.01	7.38	1.141	MgO_7
0.2330	5.98	−1.18	−1.14	8.31	1.167	2.070	0.2453	5.12	−0.97	−0.97	7.07	1.148	MgO_1
0.1994	5.15	−0.94	−0.93	7.02	1.179	2.103	0.2284	4.53	−0.86	−0.86	6.25	1.168	MgO_3
0.3724	10.29	−2.10	−2.01	14.4	1.071	1.915	0.3562	8.91	−1.78	−1.76	12.45	1.051	MgO_3
0.3126	8.49	−1.68	−1.66	11.82	1.104	1.970	0.3087	7.32	−1.42	−1.44	10.17	1.086	$Mg1O_{10}$
0.3048	8.22	−1.63	−1.60	11.45	1.111	1.980	0.3022	7.07	−1.37	−1.38	9.82	1.092	$Mg1O_1$
0.2704	7.03	−1.39	−1.35	9.77	1.142	2.028	0.2728	5.98	−1.15	−1.14	8.26	1.122	$Mg1O_7$
0.2192	5.22	−1.06	−1.01	7.29	1.207	2.123	0.2263	4.27	−0.79	−0.80	5.86	1.182	$Mg1O_6$
0.1916	4.38	−0.86	−0.83	6.07	1.245	2.180	0.2052	3.46	−0.63	−0.65	4.74	1.217	$Mg1O_6$
0.1008	1.20	−0.27	−0.13	1.61	1.433	2.836	0.0964	0.38	−0.03	−0.10	0.51	1.507	$Mg1O_7$
0.3185	8.75	−1.72	−1.70	12.16	1.098	1.961	0.3157	7.56	−1.47	−1.49	10.53	1.079	$Mg2O_3$
0.3223	8.79	−1.76	−1.72	12.27	1.099	1.961	0.3161	7.57	−1.47	−1.49	10.53	1.080	$Mg2O_{11}$
0.2289	5.53	−1.10	−1.07	7.70	1.193	2.102	0.2358	4.59	−0.86	−0.85	6.30	1.169	$Mg2O_{12}$
0.2183	5.16	−1.03	−0.99	7.18	1.210	2.128	0.2262	4.21	−0.77	−0.78	5.76	1.185	$Mg2O_8$
0.2104	4.81	−1.00	−0.94	6.74	1.228	2.151	0.2160	3.87	−0.70	−0.73	5.30	1.200	$Mg2O_4$
0.2724	7.05	−1.4	−1.38	9.84	1.141	2.026	0.2731	6.02	−1.14	−1.16	8.32	1.121	$Mg3O_2$
0.2695	7.03	−1.39	−1.37	9.80	1.141	2.026	0.2727	6.00	−1.14	−1.16	8.30	1.121	$Mg3O_9$
0.2348	5.83	−1.15	−1.12	8.10	1.179	2.083	0.2424	4.89	−0.93	−0.92	6.74	1.157	$Mg3O_5$
0.2052	4.83	−0.96	−0.93	6.72	1.223	2.147	0.2168	3.91	−0.72	−0.73	5.36	1.197	$Mg3O_8$
0.2012	4.69	−0.94	−0.91	6.53	1.228	2.156	0.2125	3.77	−0.70	−0.71	5.18	1.202	$Mg3O_4$
0.0931	1.76	−0.30	−0.28	2.35	1.440	2.481	0.1344	1.03	−0.21	−0.23	1.46	1.386	$Mg3O_{12}$
0.2291	5.45	−1.15	−1.09	7.68	1.195	2.105	0.2278	4.55	−0.84	−0.86	6.25	1.171	MgO
0.1410	2.92	−0.59	−0.57	4.09	1.304	2.357	0.1289	2.68	−0.43	−0.42	3.53	1.280	NaO_1
0.1355	2.83	−0.57	−0.54	3.94	1.303	2.363	0.1307	2.70	−0.46	−0.36	3.51	1.287	NaO_3
0.1261	2.47	−0.50	−0.46	3.43	1.337	2.412	0.1198	2.34	−0.39	−0.27	3.00	1.318	NaO_2
0.1308	2.75	−0.59	−0.56	3.90	1.307	2.368	0.1154	2.54	−0.41	−0.45	3.40	1.284	NaO(A2)
0.1142	2.26	−0.47	−0.46	3.19	1.352	2.438	0.1016	2.06	−0.36	−0.31	2.72	1.328	NaO(D)o
0.1083	2.13	−0.43	−0.43	3.00	1.365	2.459	0.0984	1.94	−0.33	−0.27	2.55	1.342	NaO(B)o
0.0918	1.74	−0.35	−0.33	2.43	1.416	2.538	0.0886	1.57	−0.26	−0.19	2.02	1.394	NaO(A1)
0.0677	1.24	−0.25	−0.21	1.71	1.495	2.665	0.0714	1.07	−0.17	−0.08	1.32	1.483	NaO(A1)
0.1239	2.77	−0.54	−0.52	3.83	1.278	2.344	0.1193	2.65	−0.47	−0.47	3.59	1.265	$Na1O_5$
0.1284	2.82	−0.57	−0.54	3.93	1.284	2.345	0.1188	2.64	−0.46	−0.47	3.58	1.266	$Na1O_2$
0.1172	2.67	−0.49	−0.48	3.65	1.275	2.348	0.1189	2.61	−0.46	−0.47	3.54	1.268	$Na1O_8$
0.1147	2.39	−0.49	−0.47	3.35	1.331	2.412	0.1036	2.18	−0.36	−0.37	2.92	1.308	$Na1O_4$
0.1012	2.02	−0.40	−0.39	2.81	1.375	2.479	0.0944	1.87	−0.31	−0.22	2.40	1.357	$Na1O_7$
0.0913	1.82	−0.35	−0.32	2.49	1.395	2.516	0.0895	1.69	−0.28	−0.17	2.14	1.383	$Na1O_8$
0.1384	3.00	−0.63	−0.60	4.22	1.281	2.332	0.1231	2.78	−0.50	−0.48	3.76	1.260	$Na2O_4$
0.1308	2.73	−0.57	−0.55	3.84	1.306	2.368	0.1167	2.55	−0.45	−0.40	3.39	1.285	$Na2O_6$
0.1080	2.26	−0.46	−0.43	3.15	1.341	2.431	0.1068	2.18	−0.24	−0.37	2.79	1.332	$Na2O_5$
0.1141	2.29	−0.45	−0.44	3.17	1.344	2.430	0.0986	2.06	−0.35	−0.34	2.75	1.318	$Na2O_6$
0.1114	2.22	−0.44	−0.42	3.08	1.348	2.440	0.1057	2.13	−0.36	−0.23	2.72	1.339	$Na2O_8$
0.1518	3.35	−0.69	−0.67	4.70	1.263	2.301	0.1345	3.09	−0.53	−0.56	4.18	1.242	$Na3O_1$
0.1356	2.85	−0.59	−0.57	4.00	1.297	2.355	0.1214	2.66	−0.41	−0.47	3.54	1.277	$Na3O_5$
0.1107	2.24	−0.45	−0.44	3.13	1.349	2.439	0.1018	2.08	−0.35	−0.29	2.72	1.329	$Na3O_2$
0.0910	1.79	−0.37	−0.34	2.50	1.397	2.517	0.0834	1.61	−0.26	−0.24	2.11	1.373	$Na3O_2$
0.1120	2.35	−0.50	−0.47	3.32	1.321	2.404	0.0993	2.20	−0.38	−0.38	2.96	1.300	NaO
0.1643	3.65	−0.73	−0.71	5.09	1.252	2.278	0.1457	3.32	−0.60	−0.57	4.49	1.227	$Na1O_1$
0.1288	2.68	−0.53	−0.51	3.72	1.318	2.384	0.1162	2.42	−0.40	−0.37	3.19	1.293	$Na1O_{10}$
0.1262	2.56	−0.50	−0.50	3.56	1.335	2.406	0.1147	2.34	−0.39	−0.31	3.04	1.311	$Na1O_{12}$
0.1118	2.15	−0.43	−0.37	2.94	1.385	2.480	0.1052	1.95	−0.31	−0.16	2.42	1.374	$Na1O_8$
0.1567	3.42	−0.68	−0.67	4.77	1.264	2.298	0.1392	3.12	−0.55	−0.53	4.20	1.240	$Na2O_9$
0.1448	3.09	−0.61	−0.60	4.30	1.287	2.334	0.1299	2.81	−0.48	−0.45	3.75	1.262	$Na2O_3$
0.1429	2.98	−0.59	−0.58	4.15	1.301	2.352	0.1283	2.73	−0.47	−0.39	3.59	1.278	$Na2O_7$
0.1224	2.37	−0.47	−0.43	3.28	1.363	2.443	0.1121	2.15	−0.35	−0.23	2.73	1.345	$Na2O_4$
0.1534	3.35	−0.67	−0.65	4.68	1.271	2.307	0.1359	3.04	−0.54	−0.51	4.09	1.246	$Na3O_{11}$
0.1397	2.90	−0.57	−0.57	4.05	1.305	2.360	0.1254	2.67	−0.46	−0.38	3.50	1.283	$Na3O_5$
0.1338	2.81	−0.56	−0.55	3.92	1.305	2.365	0.1197	2.55	−0.43	−0.41	3.39	1.281	$Na3O_2$
0.1071	2.04	−0.40	−0.36	2.80	1.396	2.498	0.1005	1.84	−0.29	−0.16	2.30	1.383	$Na3O_6$
0.1602	2.48	−0.57	−0.57	3.62	1.348	2.403	0.1242	2.21	−0.37	−0.37	2.96	1.301	NaO
1.252	24.42	−7.12	−7.05	38.60	0.905	1.529	1.2290	19.73	−5.32	−5.31	30.36	0.886	$P1O_1$
1.247	23.95	−7.07	−7.00	38.01	0.906	1.532	1.2233	19.37	−5.25	−5.26	29.87	0.888	$P1O_{10}$
1.248	23.48	−7.03	−6.96	37.47	0.907	1.533	1.2205	19.26	−5.25	−5.24	29.75	0.888	$P1O_5$
1.179	20.21	−6.44	−6.30	32.95	0.925	1.560	1.1713	15.94	−4.68	−4.69	25.31	0.906	$P1O_4$
1.265	24.84	−7.24	−7.17	39.24	0.902	1.525	1.2370	20.28	−5.40	−5.41	31.10	0.883	$P2O_9$

Table 1 (Contd.)

$\rho^{mod}(\mathbf{r}_C)$	$\nabla^2\rho(\mathbf{r}_C)^{mod}$	λ_1^{mod}	λ_2^{mod}	λ_3^{mod}	$r_b(O)^{mod}$	R(*MO*)	$\rho^{pro}(\mathbf{r}_C)$	$\nabla^2\rho(\mathbf{r}_C)^{pro}$	λ_1^{pro}	λ_2^{pro}	λ_3^{pro}	$r_b(O)^{pro}$	Bond
1.256	24.66	−7.17	−7.11	38.95	0.903	1.528	1.2315	19.94	−5.35	−5.35	30.63	0.885	$P2O_3$
1.203	21.09	−6.62	−6.51	34.22	0.919	1.551	1.1863	17.00	−4.86	−4.87	26.73	0.900	$P2O_{12}$
1.187	20.66	−6.52	−6.40	33.57	0.923	1.557	1.1774	16.38	−4.75	−4.77	25.90	0.904	$P2O_6$
1.267	25.21	−7.28	−7.22	39.71	0.901	1.524	1.2409	20.48	−5.44	−5.43	31.36	0.883	$P3O_{11}$
1.249	23.74	−7.05	−6.98	37.77	0.906	1.532	1.2225	19.34	−5.24	−5.25	29.84	0.888	$P3O_2$
1.228	22.69	−6.87	−6.80	36.35	0.911	1.540	1.2077	18.39	−5.10	−5.09	28.58	0.893	$P3O_7$
1.179	20.35	−6.43	−6.32	33.10	0.924	1.560	1.1723	16.02	−4.70	−4.71	25.43	0.905	$P3O_8$
1.275	27.63	−7.65	−7.58	42.86	0.893	1.512	1.2584	22.06	−5.71	−5.72	33.48	0.875	PO_2
1.255	26.52	−7.40	−7.37	41.29	0.898	1.520	1.2429	21.03	−5.54	−5.53	32.10	0.880	PO_1
0.9948	22.72	−6.31	−6.28	35.31	0.947	1.614	0.8537	19.15	−4.20	−4.20	27.55	0.921	SiO_1
0.9689	20.77	−5.93	−5.85	32.55	0.962	1.635	0.8285	17.39	−3.83	−3.81	25.03	0.935	SiO_3
0.9332	19.48	−5.62	−5.51	30.61	0.973	1.651	0.8071	16.11	−3.56	−3.56	23.24	0.946	SiO_2
0.9775	22.03	−6.35	−6.14	34.52	0.954	1.623	0.8379	18.40	−4.03	−4.06	26.49	0.927	SiO_1
0.9508	21.32	−6.11	−5.87	33.30	0.960	1.632	0.8235	17.65	−3.91	−3.89	25.45	0.933	SiO_4
0.9514	20.83	−6.10	−5.90	32.83	0.963	1.636	0.8185	17.33	−3.80	−3.85	24.98	0.936	SiO_3
0.9431	20.44	−6.02	−5.78	32.24	0.965	1.640	0.8141	17.03	−3.74	−3.78	24.55	0.938	SiO_2
0.9884	22.82	−6.49	−6.29	35.60	0.951	1.618	0.8488	18.87	−4.09	−4.15	27.12	0.923	SiO_3
0.9654	21.24	−6.23	−5.98	33.45	0.958	1.630	0.8282	17.83	−3.95	−3.91	25.70	0.931	SiO_4
0.9301	19.90	−5.93	−5.74	31.56	0.969	1.646	0.8045	16.53	−3.67	−3.67	23.87	0.942	SiO_2
0.9705	21.68	−6.12	−6.04	33.85	0.956	1.627	0.8350	18.07	−3.99	−3.94	26.00	0.929	SiO
1.073	27.63	−7.01	−6.95	41.59	0.918	1.574	0.9216	22.93	−4.99	−4.97	32.89	0.893	SiO_3
0.9388	20.56	−5.99	−5.85	32.40	0.966	1.640	0.8111	16.94	−3.77	−3.74	24.46	0.938	SiO_1
0.9224	20.05	−5.94	−5.72	31.71	0.969	1.645	0.8058	16.60	−3.67	−3.71	23.97	0.942	SiO_4
0.9375	20.66	−6.03	−5.76	32.45	0.964	1.638	0.8118	17.10	−3.81	−3.80	24.7	0.937	SiO_1
0.9330	20.24	−5.97	−5.77	31.98	0.967	1.642	0.8072	16.80	−3.75	−3.72	24.27	0.940	SiO_3
0.9223	19.75	−5.85	−5.65	31.25	0.970	1.647	0.7993	16.41	−3.68	−3.66	23.74	0.943	SiO_2
0.8433	17.88	−5.22	−5.06	28.15	0.987	1.673	0.7654	14.39	−3.26	−3.30	20.95	0.960	$Si2O_6$
0.9338	21.07	−6.00	−5.88	32.95	0.960	1.634	0.8191	17.44	−3.87	−3.85	25.16	0.934	$Si1O_5$
1.072	25.61	−6.81	−6.77	39.18	0.928	1.587	0.9009	21.65	−4.72	−4.70	31.06	0.902	$Si2O_4$
1.036	23.96	−6.55	−6.54	37.05	0.939	1.602	0.8729	20.24	−4.40	−4.41	29.05	0.913	$Si1O_1$
1.002	22.40	−6.28	−6.24	34.92	0.949	1.617	0.8439	18.90	−4.14	−4.16	27.20	0.923	$Si1O_7$
0.9645	22.80	−6.27	−6.18	35.25	0.948	1.617	0.8495	18.96	−4.17	−4.16	27.28	0.922	$Si2O_2$
0.9362	21.39	−6.04	−5.91	33.35	0.958	1.631	0.8243	17.69	−3.91	−3.90	25.51	0.932	$Si1O_6$
0.8811	19.33	−5.55	−5.49	30.38	0.974	1.655	0.7884	15.80	−3.57	−3.53	22.90	0.948	$Si2O_5$
0.8219	16.72	−5.01	−4.84	26.57	0.997	1.688	0.7506	13.39	−3.08	−3.10	19.56	0.969	SiO_6
0.8636	18.49	−5.39	−5.32	29.19	0.981	1.664	0.7789	15.05	−3.41	−3.39	21.86	0.954	SiO_6
1.035	23.79	−6.56	−6.52	36.87	0.939	1.602	0.8743	20.19	−4.41	−4.41	29.02	0.913	SiO_6
1.080	25.85	−6.84	−6.81	39.50	0.927	1.585	0.9061	21.87	−4.76	−4.74	31.37	0.901	SiO_6
0.9651	21.26	−6.26	−5.99	33.50	0.959	1.631	0.8278	17.79	−3.93	−3.89	25.61	0.932	SiO_1
0.9644	21.32	−6.24	−5.97	33.54	0.960	1.631	0.8274	17.76	−3.89	−3.91	25.57	0.933	SiO_2
0.9541	20.75	−6.16	−5.90	32.81	0.963	1.636	0.8197	17.37	−3.85	−3.81	25.03	0.936	SiO_3
1.053	25.54	−6.78	−6.70	39.02	0.929	1.589	0.8944	21.41	−4.67	−4.65	30.74	0.904	SiO_2
0.9372	21.84	−6.07	−5.98	33.89	0.956	1.628	0.8311	17.96	−3.97	−3.95	25.87	0.930	SiO_3
0.9222	21.05	−5.93	−5.81	32.79	0.962	1.636	0.8195	17.29	−3.83	−3.81	24.93	0.936	SiO_3
0.9521	20.62	−6.07	−5.90	32.59	0.964	1.637	0.8178	17.21	−3.82	−3.80	24.83	0.936	SiO_1
1.055	25.83	−6.84	−6.79	39.46	0.928	1.587	0.8981	21.61	−4.71	−4.69	31.01	0.902	SiO_2
0.9472	22.25	−6.20	−6.07	34.51	0.953	1.624	0.8367	18.33	−4.04	−4.02	26.39	0.927	SiO_3
0.9431	21.96	−6.13	−6.05	34.13	0.955	1.627	0.8339	18.09	−3.96	−3.99	26.04	0.929	SiO_3
0.9468	20.44	−6.01	−5.90	32.35	0.965	1.639	0.8147	17.05	−3.79	−3.77	24.61	0.938	SiO_1
0.9797	22.68	−6.45	−6.22	35.35	0.951	1.619	0.8418	18.75	−4.10	−4.13	26.99	0.924	SiO_2
0.9909	25.21	−6.59	−6.57	38.37	0.932	1.595	0.8791	20.84	−4.54	−4.54	29.93	0.908	SiO_1
0.9936	25.36	−6.61	−6.60	38.57	0.931	1.594	0.8806	20.96	−4.57	−4.58	30.11	0.907	SiO_1
1.013	23.98	−6.55	−6.41	36.94	0.940	1.604	0.8655	20.01	−4.37	−4.39	28.77	0.914	Si2mO(D)o
0.9848	24.64	−6.48	−6.45	37.58	0.935	1.600	0.8702	20.39	−4.46	−4.45	29.31	0.911	Si1mO(B)m
1.019	24.12	−6.60	−6.55	37.27	0.939	1.602	0.8692	20.22	−4.42	−4.42	29.05	0.913	Si1mO(A1)
0.9452	22.72	−6.12	−6.06	34.90	0.949	1.619	0.8394	18.68	−4.12	−4.10	26.90	0.924	Si1mO(D)m
0.9543	22.35	−6.23	−6.06	34.64	0.952	1.622	0.8352	18.47	−4.06	−4.08	26.61	0.926	Si1mO(C)m
0.9515	22.97	−6.17	−6.08	35.22	0.947	1.617	0.8429	18.89	−4.16	−4.15	27.20	0.922	Si2oO(D)m
1.040	25.21	−6.76	−6.64	38.61	0.932	1.593	0.8846	21.08	−4.60	−4.59	30.27	0.906	Si2oO(B)o
0.9645	22.59	−6.29	−6.19	35.06	0.950	1.619	0.8407	18.75	−4.11	−4.13	26.99	0.924	Si2oO(C)m
0.9386	21.06	−6.10	−5.95	33.10	0.961	1.634	0.8177	17.44	−3.84	−3.87	25.16	0.934	Si2oO(A2)
0.9111	20.29	−5.86	−5.75	31.91	0.968	1.644	0.8034	16.64	−3.69	−3.72	24.04	0.941	Si2mO(A2)
1.030	24.22	−6.65	−6.56	37.43	0.938	1.600	0.8725	20.38	−4.44	−4.46	29.28	0.911	Si2mO(C)o
0.9388	22.92	−6.08	−6.01	35.02	0.948	1.618	0.8410	18.76	−4.13	−4.12	27.01	0.923	Si2mO(B)m
1.007	25.49	−6.66	−6.63	38.77	0.930	1.592	0.8853	21.13	−4.62	−4.60	30.35	0.906	Si1mObm
1.003	22.93	−6.35	−6.31	35.59	0.946	1.613	0.8520	19.25	−4.23	−4.22	27.70	0.92	Si1mOa1
0.9606	23.06	−6.24	−6.16	35.46	0.947	1.616	0.8467	19.00	−4.18	−4.16	27.34	0.922	Si1mOdm
0.8817	18.83	−5.55	−5.38	29.75	0.978	1.660	0.7792	15.40	−3.46	−3.49	22.36	0.951	Si1mOcm

Table 1 (Contd.)

$\rho^{mod}(\mathbf{r}_C)$	$\nabla^2\rho(\mathbf{r}_C)^{mod}$	λ_1^{mod}	λ_2^{mod}	λ_3^{mod}	$r_b(O)^{mod}$	R(*M*O)	$\rho^{pro}(\mathbf{r}_C)$	$\nabla^2\rho(\mathbf{r}_C)^{pro}$	λ_1^{pro}	λ_2^{pro}	λ_3^{pro}	$r_b(O)^{pro}$	Bond
1.013	24.14	−6.52	−6.41	37.08	0.939	1.603	0.8676	20.12	−4.40	−4.41	28.93	0.913	Si2mOdo
0.9256	21.56	−5.96	−5.84	33.35	0.958	1.631	0.8211	17.65	−3.91	−3.91	25.47	0.932	Si2oOdm
1.037	25.91	−7.00	−6.85	39.75	0.929	1.588	0.8953	21.55	−4.66	−4.69	30.90	0.903	Si2oOcm
1.033	25.17	−6.66	−6.58	38.41	0.933	1.594	0.8830	20.96	−4.58	−4.57	30.11	0.907	Si2oObo
0.9701	23.21	−6.40	−6.30	35.91	0.946	1.614	0.8508	19.16	−4.19	−4.21	27.56	0.921	Si2oOa2
1.042	24.66	−6.74	−6.65	38.05	0.935	1.596	0.8807	20.75	−4.51	−4.54	29.80	0.909	Si2mOco
0.9569	22.93	−6.30	−6.23	35.46	0.949	1.618	0.8454	18.85	−4.12	−4.15	27.12	0.923	Si2mOa2
0.8981	20.91	−5.73	−5.66	32.30	0.962	1.639	0.8094	17.01	−3.79	−3.79	24.59	0.937	Si2mObm
0.9771	22.63	−6.40	−6.13	35.16	0.950	1.619	0.8412	18.75	−4.13	−4.11	26.98	0.924	SiO
0.9757	22.01	−6.39	−6.13	34.53	0.955	1.624	0.8360	18.33	−4.02	−4.03	26.38	0.927	SiO
0.9929	22.95	−6.55	−6.30	35.79	0.948	1.615	0.8499	19.10	−4.20	−4.16	27.46	0.922	SiO
0.967	22.98	−6.32	−6.23	35.53	0.947	1.616	0.8460	19.00	−4.16	−4.18	27.34	0.922	SiO
0.9612	20.93	−5.95	−5.92	32.80	0.959	1.632	0.8240	17.64	−3.89	−3.90	25.44	0.933	$Si1O_4$
0.9433	20.21	−5.77	−5.77	31.74	0.963	1.638	0.8127	17.09	−3.79	−3.80	24.68	0.937	$Si1O_3$
0.8062	15.53	−4.89	−4.68	25.09	1.007	1.701	0.7284	12.47	−2.93	−2.91	18.31	0.979	$Si1O_2$
1.051	24.24	−6.55	−6.51	37.30	0.935	1.597	0.8825	20.60	−4.50	−4.50	29.61	0.909	SiO_2
1.006	22.46	−6.29	−6.24	34.99	0.950	1.617	0.8561	18.88	−4.13	−4.12	27.14	0.923	SiO_3
0.8725	19.65	−5.54	−5.39	30.58	0.975	1.655	0.7977	15.76	−3.52	−3.51	22.80	0.948	SiO_1
0.990	24.31	−6.57	−6.46	37.35	0.938	1.603	0.8652	20.18	−4.42	−4.41	29.00	0.913	SiO
0.9852	24.29	−6.48	−6.43	37.20	0.938	1.603	0.8640	20.11	−4.39	−4.40	28.90	0.914	SiO
0.9884	24.05	−6.56	−6.41	37.02	0.939	1.605	0.8618	19.99	−4.37	−4.38	28.74	0.914	SiO
0.9669	23.19	−6.31	−6.24	35.74	0.946	1.614	0.8466	19.18	−4.20	−4.21	27.60	0.920	SiO
1.966	24.80	−11.81	−11.75	48.36	0.876	1.447	1.7662	14.61	−7.13	−7.09	28.83	0.841	$S1O_4$
1.895	23.47	−11.19	−11.13	45.79	0.886	1.460	1.7333	12.12	−6.75	−6.77	25.64	0.848	$S1O_3$
1.890	19.26	−10.99	−10.97	41.22	0.893	1.472	1.7049	10.11	−6.48	−6.54	23.13	0.853	$S1O_2$
1.826	18.02	−10.61	−10.48	39.11	0.903	1.485	1.6749	7.98	−6.26	−6.26	20.50	0.859	$S1O_1$
1.957	23.56	−11.67	−11.59	46.82	0.879	1.451	1.7568	13.83	−7.00	−7.02	27.85	0.843	$S2O_6$
1.925	21.93	−11.36	−11.28	44.58	0.885	1.460	1.7357	12.18	−6.75	−6.77	25.70	0.848	$S2O_8$
1.865	17.32	−10.70	−10.68	38.69	0.899	1.481	1.6852	8.56	−6.35	−6.34	21.26	0.857	$S2O_5$
1.832	17.15	−10.59	−10.47	38.21	0.905	1.488	1.6715	7.64	−6.20	−6.24	20.08	0.860	$S2O_7$
1.880	19.98	−11.03	−10.82	41.83	0.894	1.472	1.7077	10.11	−6.53	−6.48	23.12	0.854	SO_2
1.884	19.20	−11.12	−10.77	41.09	0.894	1.473	1.7046	9.91	−6.48	−6.50	22.90	0.854	SO_1

Bond-critical point property systematics for procrystal and model electron-density distributions

Of the more than 300 nonequivalent bond paths and bond-critical points displayed by the $\rho(\mathbf{r}_C)^{mod}$ distributions generated for the silicates and oxides (Gibbs et al. 2001), each is displayed by its $\rho(\mathbf{r}_C)^{pro}$ representatives. As found for the model electron-density distributions, the bond paths are nearly straight. Also, the bonded radii displayed by the model distributions are in close agreement and highly correlated with those calculated for the procrystal distributions (Fig. 2). As observed for a number of hydroxyacid molecules (Hill et al. 1997), the $r_b(O)$ values for both model and procrystal electron-density distributions range between 0.65 Å (the atomic radius of the oxygen atom) and 1.45 Å (the ionic radius of the oxide anion). The fact that $r_b(O)^{pro}$ and $r_b(O)^{mod}$ exhibit the same range of values suggests that the positions of the bcps and the bonded radii themselves are governed, in large part, by the atomic character of the electron-density distributions. As the data in Fig. 2 are systematically displaced from the 45° line in the direction of larger $r_b(O)^{mod}$ values, the bonded radii of the oxide anion exhibited for the model distributions are, on average, slightly larger than those exhibited by the procrystal distributions. Moreover, $r_b(O)^{mod}$ for the oxide anions bonded to second-row *M* atoms tend to be systematically displaced to a greater extent from the line (0.02 Å) than those for anions bonded to first-row *M* atoms (0.01 Å). This re-

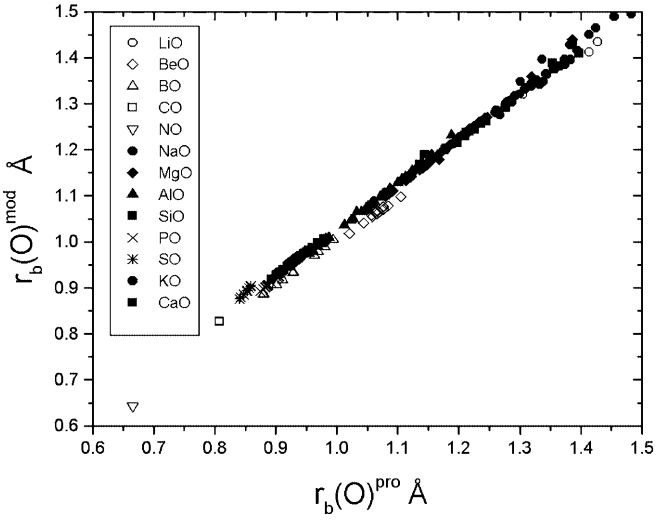

Fig. 2 The bonded radius of the O atom determined from procrystal calculations, $r_b(O)^{pro}$, versus that determined from ab initio model calculations, $r_b(O)^{mod}$, for more than 300 *M*O bonds in minerals. The trend of the data demonstrates not only that the procrystal model reproduces all bond critical points found in the ab initio model calculations, but also the similarity in their locations

sult indicates that the oxide anions of the model structures have slightly larger radii (0.01 to 0.02 Å) than those exhibited by the procrystal structures. It also suggests that the redistribution of electron density in the model structure relative to that of the procrystal is very small but systematic, resulting in a displacement of the bcp in the direction of the *M* cations. This observation is consistent with a small buildup of electron density in the basin of the O atoms at the expense of the cations.

The $\rho(\mathbf{r}_C)^{mod}$ values calculated for the silicate and oxide materials are plotted against $\rho(\mathbf{r}_C)^{pro}$ in Fig. 3. For each of the *M*O-bonded interactions, $\rho(\mathbf{r}_C)^{mod}$ is highly correlated with $\rho(\mathbf{r}_C)^{pro}$, with R^2 values ranging between 0.93 for the NaO bond and 0.99 for the AlO bond. The values of $\rho(\mathbf{r}_C)^{mod}$ range from similar to larger than those for $\rho(\mathbf{r}_C)^{pro}$, with the difference tending to increase as the electronegativity of the *M* cation tends to increase. For the more electronegative cations, the $\rho(\mathbf{r}_C)^{mod}$ values tend to be 0.2 to 0.4 e Å^{-3} larger than the $\rho(\mathbf{r}_C)^{pro}$ values, whereas for the more electropositive cations (Li, Na, K, Ca, Al), the $\rho(\mathbf{r}_C)^{mod}$ values tend to be only slightly larger (0.01 to 0.02 e Å^{-3}) than the corresponding $\rho(\mathbf{r}_C)^{pro}$ values. In contrast, $\rho(\mathbf{r}_C)^{mod}$ values for the MgO and PO bonded interactions are slightly smaller by 0.01 e Å^{-3}, on average, than the $\rho(\mathbf{r}_C)^{pro}$ values. The closer agreement between $\rho(\mathbf{r}_C)^{mod}$ and $\rho(\mathbf{r}_C)^{pro}$ for the more electropositive cations suggests that the cations comprising these bonded interactions have substantial atomic character and behave as if largely neutral, in agreement with Pauling and Slater's electroneutrality principle. Given the large electronegativity of the P atom, it is not clear why $\rho(\mathbf{r}_C)^{mod}$ and $\rho(\mathbf{r}_C)^{pro}$ tend to be identical for the PO-bonded interactions. Furthermore, a calculation (Gibbs et al. 2001) of $\rho(\mathbf{r}_C)$ values for the PO bonds of a number of molecules yielded values that are ~0.3 e Å^{-3} larger, on average, than the $\rho(\mathbf{r}_C)^{mod}$ values while $\rho(\mathbf{r}_C)^{mod}$ values for other bonds were found to be in good agreement with the molecular $\rho(\mathbf{r}_C)$ values. This discrepancy suggests that the basis set used to model the wave functions of the P atom in the CRYSTAL98 calculations may not be as robust as the other basis sets used in the calculations, or that there is a fundamental difference in the electron-density distribution around the P atom.

As displayed in Fig. 4, the average curvatures, $\lambda_{1,2}$, of the model electron-density distributions for each of the *M*O bonds are significantly greater than the average curvatures calculated for the procrystal electron distributions, but still highly correlated. In general, it is observed that differences between $\lambda_{1,2}^{mod}$ and $\lambda_{1,2}^{pro}$ are greater for *M* cations with large electronegativities. For the more electropositive cations, the $\lambda_{1,2}^{mod}$ values are very similar to the $\lambda_{1,2}^{pro}$ values. Not only does the value of $\rho(\mathbf{r}_C)^{mod}$ increase relative to $\rho(\mathbf{r}_C)^{pro}$ with the increasing electronegativity of the *M* cation, but also the maxima in $\rho(\mathbf{r}_C)^{mod}$ perpendicular to the bond paths becomes progressively sharper relative to maxima displayed by the $\rho(\mathbf{r}_C)^{pro}$ distributions.

The curvatures of the model electron-density distributions at the minima along the paths for each of the *M*O bonds, λ_3^{mod}, are likewise highly correlated with λ_3^{pro}, with the minima becoming progressively sharper with decreasing bond length (Fig. 5). In each case, λ_3^{mod} is larger than λ_3^{pro}. Although not perfect, there is a tendency for the λ_3^{mod} curvatures for *M*O-bonded interactions involving second-row cations to be larger than those for bonded interactions involving first-row cations. The λ_3^{mod} curvatures calculated for the SO bonds are substantially larger than the λ_3^{pro} curvatures for the

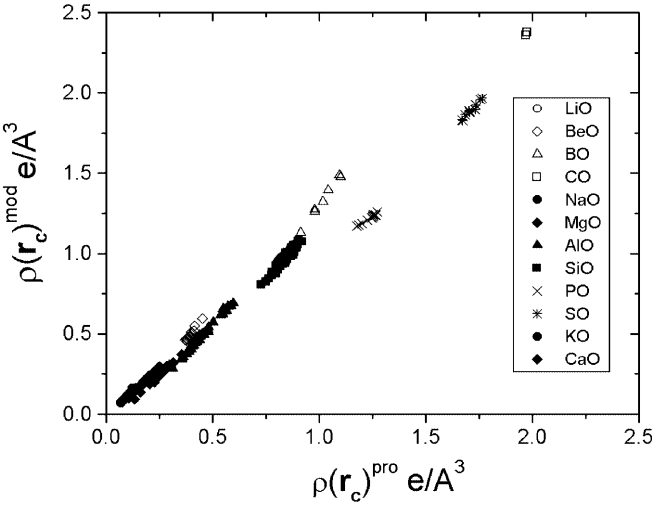

Fig. 3 The magnitude of the electron density at the bond-critical point computed with the procrystal calculations, $\rho(\mathbf{r}_C)^{pro}$, compared to that computed with the ab initio model, $\rho(\mathbf{r}_C)^{mod}$. The data demonstrate that $\rho(\mathbf{r}_C)^{mod}$ tends to be larger than $\rho(\mathbf{r}_C)^{pro}$, with a systematically increasing difference displayed by bonds with electronegative cations

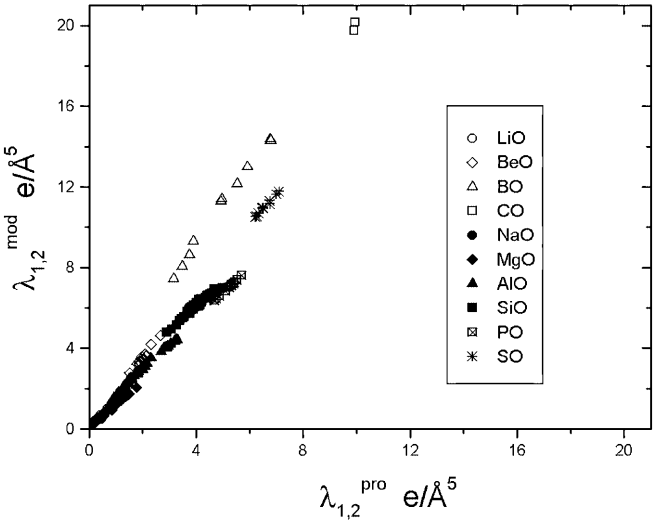

Fig. 4 The average curvatures of the electron density at the bond-critical point in the plane perpendicular to the bond are compared for the procrystal, $\lambda_{1,2}^{pro}$, and the ab initio model calculations, $\lambda_{1,2}^{mod}$. The values of $\lambda_{1,2}^{mod}$ tend to be larger than $\lambda_{1,2}^{pro}$, with a difference related to the electronegativity of the bonded cation. Note that while the values of $\lambda_{1,2}$ are actually negative, we plot the curvatures as positive

other bonded interactions. Thus, with increasing covalent character, the electron density in the model structures is progressively localized between the bonded atoms relative to the representative procrystal model.

In as much as $\lambda_{1,2}^{pro}$ correlates linearly with $\lambda_{1,2}^{mod}$ (Fig. 4) and λ_3^{pro} correlates linearly with λ_3^{mod} (Fig. 5) for each of the bonded interactions, it follows that $\nabla^2\rho(\mathbf{r}_C)^{pro}$ must also correlate linearly with $\nabla^2\rho(\mathbf{r}_C)^{mod}$, as displayed in Fig. 6. For the most part, the $\nabla^2\rho(\mathbf{r}_C)$ data are distributed in two separate regions in Fig. 6, with $\nabla^2\rho(\mathbf{r}_C)^{pro}$ greater than $\nabla^2\rho(\mathbf{r}_C)^{mod}$ for bonded interactions involving first-row atoms while $\nabla^2\rho(\mathbf{r}_C)^{mod}$ is greater than $\nabla^2\rho(\mathbf{r}_C)^{pro}$ for interactions involving second-row atoms. Interestingly, some researchers (Bader 1990) have related bond character to $\nabla^2\rho(\mathbf{r}_C)$, suggesting that larger values of $\nabla^2\rho(\mathbf{r}_C)$ indicate a greater degree of ionicity. Since the procrystal representation does not include the migration of electron density, our results suggest that the bond character is not directly or, at least, simply, related to the Laplacian. Furthermore, since the greatest differences between ab initio and the procrystal models seem to be related to the curvatures perpendicular to the bond, this study demonstrates that the true migration of electron density in a real crystal occurs from the directions perpendicular to a bond, and not along a bond; for instance, not from a cation towards an anion.

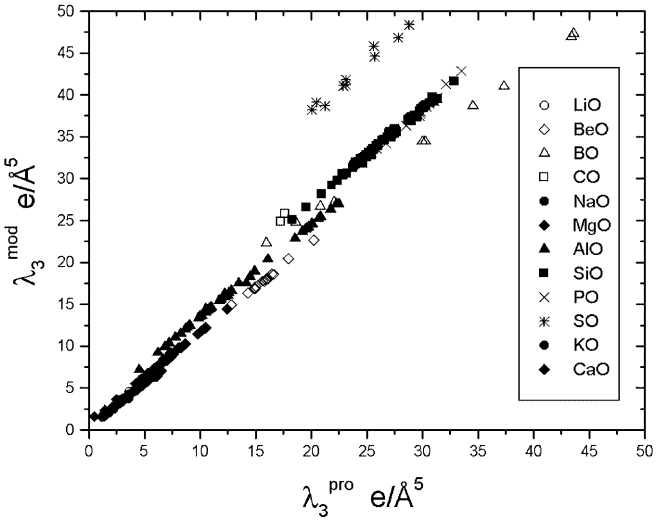

Fig. 5 The curvatures of the electron density at the bond-critical point in the direction parallel to the bond are compared for the procrystal, λ_3^{pro}, and the ab initio model calculations, λ_3^{mod}

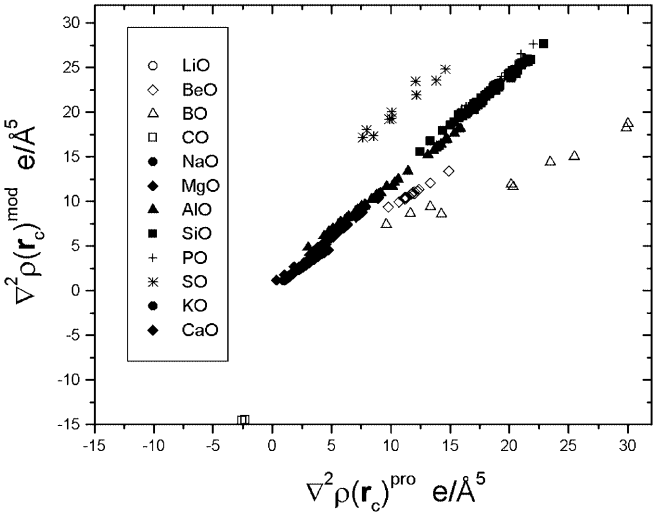

Fig. 6 The Laplacian of the electron density at the bond-critical points are compared for the procrystal, $\nabla^2\rho(\mathbf{r}_C)^{pro}$, and the ab initio model calculations, $\nabla^2\rho(\mathbf{r}_C)^{mod}$. This is a measure of the local concentration or depletion of electron density at the bond-critical point. Several well-developed trends emerge, with $\nabla^2\rho(\mathbf{r}_C)^{pro} > \nabla^2\rho(\mathbf{r}_C)^{mod}$ for bonds with first-row cations, while the reverse holds for bonds with second-row cations

Examples

Several examples will now be given to illustrate how a procrystal representation of the electron-density distribution of a material can be used as a tool to shed light on its bonded interactions, coordination numbers, and bonded radii. Examples will also be given where a procrystal representation utterly fails as a tool to identify bonded interactions that are susceptible to rupture and to determine sites of potential electrophilic attack and reactivity.

A comparison of observed and procrystal bcp properties

A map of the bcp properties observed for danburite, $CaB_2Si_2O_8$, (Downs and Swope 1992) displays bond paths radiating from each Ca cation to seven oxide anions, indicating that the cation is seven-coordinated. A calculation of the bcp properties for a procrystal representation of the electron-density distribution yields the same number of bond-critical points and bond paths. The positions of the bcps along the bond paths for the two distributions are very similar, as also observed for the alkali halides (Tsirelson et al. 1998a). In addition, as observed above for bonded interactions involving the more electropositive cations, the average value of $\rho(\mathbf{r}_C)^{pro}$, 0.17 e Å^{-3}, calculated for danburite, is in close agreement with that observed for the CaO bond, 0.16 e Å^{-3}; The average value of $r_b(O)^{pro}$, 1.21 Å, is likewise in close agreement with observed bonded radius of the anion, 1.22 Å (Gibbs et al. 1992). The correlation between R(CaO) and the observed values of $\rho(\mathbf{r}_C)$ and that between R(CaO) and $\rho(\mathbf{r}_C)^{pro}$ are not only well developed, but similar.

SiO-bonded interactions and a signature of bonds susceptible to rupture

In a careful determination of the crystal structure of triclinic $CaSi_2O_5$, Angel et al. (1996) concluded, on the

basis of the ^{29}Si NMR spectra and empirical bond valences, that the Si cations in the material are not only four- and six-coordinated by oxide anions but also five-coordinated, unlike the monoclinic form which only has four- and six-coordinated Si (Angel 1997). Relative to the six-coordinate Si in the monoclinic form, one of the oxide anions, denoted O2ox in the triclinic form, is at a distance of 2.83 Å from the Si cation, denoted here as the ^{V}Si cation, resulting in a distorted SiO_5 square-pyramidal coordination polyhedron. On the basis of the small bond valence value calculated for the bond, 0.04 e, Angel et al. (1996) concluded, "there is no significant bonding between the silicon and the O2ox oxygen." Warren et al. (1999) continued the study with a modeling of the transformation between the monoclinic form with four- and six-coordinated Si and the triclinic form with four-, five- and six-coordinated Si. With a completion of first-principle calculations and a Mulliken bond-overlap population analysis, they concluded that the ^{V}Si cation is strongly bonded to five oxide anions with bond-overlap populations, n(SiO), ranging between 0.60 and 0.97. As the n(SiO) value for the linkage between the ^{V}Si cation and the distant O2x anion is 0.05, a weak bonded interaction is indicated to exist between the two atoms. However, in their study, the n(CaO) values, calculated for the two-nonequivalent CaO_8-coordinated polyhedra in the triclinic form, were found to be unrealistically negative, indicating a weak antibonding repulsive interaction between the Ca cations and each of the coordinating anions.

To further our understanding of the bonded interactions, the electron-density distribution and the bcp properties were calculated with the CRYSTAL98 software for the triclinic form with the strategies used by Gibbs et al. (2001). These calculations show that eight bond paths radiate from each Ca cation, four from two of the Si cations, and six from those remaining. Of the six radiating from the ^{V}Si cation, one extends ~2.83 Å to O2ox and the remaining five terminate on the oxide anions comprising the square pyramid. The $\rho(\mathbf{r}_C)$ values for the bonds comprising the square pyramid range between 0.67 and 0.99 e Å^{-3} while that for ^{V}SiO2ox interaction is much smaller, 0.10 e Å^{-3}. Clearly, as concluded by Warren et al. (1999), the ^{V}SiO2ox-bonded interaction is relatively weak. However, the ellipticity, ε, of the bond is exceptionally large, 3.55 (a signature of an impending disassociation of the bond), indicating that the electron density along the bond path is highly anisotropic in cross-section and that the bonded interaction is on the verge of rupturing. The $\rho(\mathbf{r}_C)$ values for the CaO-bonded interactions range between 0.08 and 0.30 e Å^{-3} with an average value of 0.22 e Å^{-3}. On the basis of these values, the CaO-bonded interactions are indicated to range between being weak to moderate in strength. A calculation of $\rho(\mathbf{r})^{pro}$ for the triclinic form of $CaSi_2O_5$ reproduces all of the bond-critical points and bond paths found for the $\rho(\mathbf{r})^{mod}$ distribution, including those involved in the ^{V}SiO2ox-bonded interaction. The value of $\rho(\mathbf{r}_C)^{pro}$ for the interaction, 0.15 e Å^{-3}, is somewhat larger than that obtained for $\rho(\mathbf{r}_C)^{mod}$. However, because of the nature of the procrystal model, its calculated ellipticities are small (0.05 compared to 3.55) and therefore the $\rho(\mathbf{r}_C)^{pro}$ distribution provides little information about the stability of bonded interactions. Similarly, the procrystal model is expected to provide little information about the π character of a bonded interaction.

Lone-pair domains of electrons in low albite: potential sites of chemical activity

Procrystal electron-density distributions for low albite, determined at pressures between ambient conditions and 3.78 GPa, not only display bond paths that connect each Na with five oxide anions, but also show that the connections remain intact over the pressure range studied (Downs et al. 1996). Model electron-density distributions for the feldspar yield the same set of paths and bond-critical points (Gibbs et al. 2001). They did not, however, reveal any evidence for a structural change as reported for low microcline at pressures to 7 GPa (Allan and Angel 1997). However, when studied at high P_{H_2O}, Goldsmith (1986) reported a change in low albite that he ascribed to an incipient migration and diffusion of the Al and Si cations. In a discussion of the structural properties of the feldspar based on a five-coordinated Na atom, Downs et al. (1994) suggested that the diffusion process was very likely initiated by the electrophilic attack of H^+ or the hydronium ion on the underbonded O_{CO} oxide anion with a concomitant rupturing of the AlO and SiO bonds and the subsequent release and diffusion of Al and Si cations in the structure (Xiao 1994).

In an examination of the reaction, the sites of potential attack for the oxide anions of low albite were recently highlighted in a CRYSTAL98 calculation of the $-\nabla^2\rho(\mathbf{r}_C)^{mod}$ distribution for the feldspar (Gibbs et al. 2001). The calculation revealed that the distribution of the valence shell electrons for O_{CO}, unlike that of the other two-coordinated anions in the structure, displays maxima in the distribution that can be ascribed to two domains of lone-paired electrons, making the pair a potential site for electrophilic attack (cf. Bader et al. 1984; Bader and MacDougall 1985; MacDougall 1989). With protonation of the O_{CO} anion, the AlO_{CO} and SiO_{CO} bonds would certainly increase in length (Xiao 1994), accompanied by a substantial bond weakening. The end result would most likely be an impending rupture of the bonds, cation diffusion, and disorder of Al and Si.

The maxima displayed in the $-\nabla^2\rho(\mathbf{r})^{mod}$ distribution for low albite provide support for the Downs et al. (1994) picture that the O_{CO} anion plays a pivotal role in governing the diffusion and disorder of the Al and Si cations at high P_{H_2O}. However, because a procrystal electron-density distribution is simply additive, $\rho(\mathbf{r})^{pro}$ will be devoid of domains of locally concentrated electron density ascribed to lone-pair electrons, which can

be sites of potential electrophilic attack (MacDougall 1989). As an illustration of this fact, relief maps of $-\nabla^2\rho(\mathbf{r})^{pro}$ and $-\nabla^2\rho(\mathbf{r})^{mod}$ distributions for the $H_6Si_2O_7$ molecule, calculated in a plane section passing through the SiOSi bridge of the molecule, are displayed in Fig. 7. Both maps exhibit a spike-like local concentration of electron density (representing the core electrons) at the positions of the oxygen nuclei. The outer shell represents the local concentration of electron density of the valence shell of the oxygen atom (cf. Bader 1990). In the case of the $-\nabla^2\rho(\mathbf{r})^{mod}$ relief map, the valence shell local concentration of electron density displays three maxima, defining domains of local concentration of electron density. The two smaller maxima along the SiO bond vectors are ascribed to domains of bond-pair electrons while the larger one at the apex of the SiOSi angle is ascribed to a domain of lone-pair electrons (Gibbs et al. 2001). In the $-\nabla^2\rho(\mathbf{r})^{pro}$ relief map, a valence shell local concentration for the oxide anion is uniform and devoid of maxima, illustrating that a $-\nabla^2\rho(\mathbf{r})^{pro}$ distribution cannot, as observed above, be used to highlight domains of lone-pair electrons and sites of potential electrophilic attack.

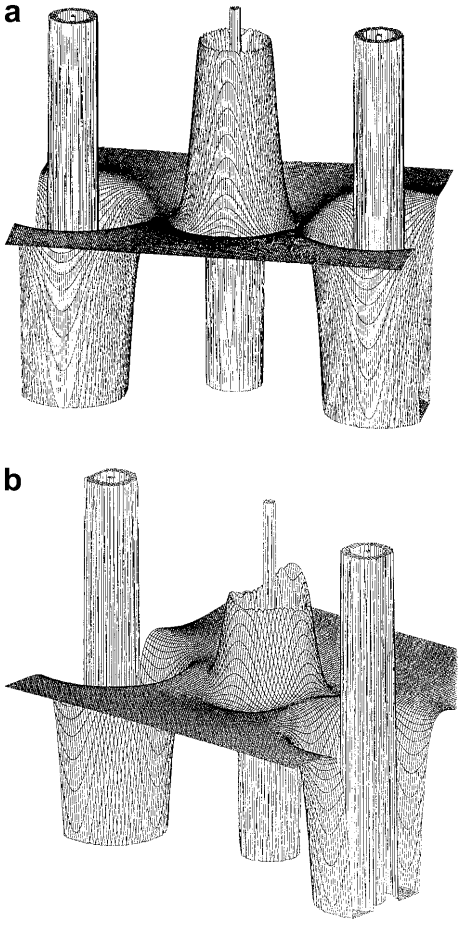

Fig. 7a, b A surface contour map of the negative of the Laplacian of the electron density, $-\nabla^2\rho(\mathbf{r})$ in the SiOSi plane of the $H_6Si_2O_7$ molecule computed with **a** the procrystal, and **b** the ab initio models. This figure demonstrates that the procrystal model cannot be used to determine domains of lone-pair electrons and sites of potential electrophilic attack

Phase transformations of clinopyroxenes as a function of pressure and temperature

High-quality single-crystal X-ray diffraction experiments have recently provided details of pressure- and temperature-induced changes in the crystal structures of the pyroxenes kanoite (nominally $MnMgSi_2O_6$) (Arlt and Armbruster 1997; Arlt et al. 1998) and clinoferrosilite ($Fe_2Si_2O_6$) (Sueno et al. 1984; Hugh-Jones et al. 1994).

Kanoite displays $P2_1/c$ symmetry at room conditions but transforms to $C2/c$ at temperatures above 240 °C, denoted HT $C2/c$, or at pressures greater than 5 GPa, denoted HP $C2/c$. In a comparison of the structure of HP and HT $C2/c$ kanoite, Arlt et al. (1998) remarked that the O3–O3–O3 angles are significantly different, 175° for HT and 140° for HP. As this change is "much larger than any changes [that] have been reported to occur as continuous changes in a clinopyroxene as a result of changes in P and/or T without phase transitions", Arlt et al. (1998) conclude that the two $C2/c$ structures must represent distinct phases.

In a similar way, ferrosilite also adopts an HT $C2/c$ structure when the *Pbca* orthoferrosilite structure is heated above 1025 °C (Sueno et al. 1984) and it adopts an HP $C2/c$ structure if the $P2_1/c$ structure is compressed to pressures above 1.75 GPa (Hugh-Jones et al. 1994). Sueno et al. (1984) recognized that the bonded interactions of the $M2$ cation to bridging O3 atoms might be "one of the motive forces for the ortho–clino transition", and that an understanding of the mechanism of the transition would require a study of the bonding distribution around the $M2$ site. For this reason, the electron-density distribution for both of these pyroxenes was computed with crystal and procrystal models, one set of calculations representing the $P2_1/c$ structure, one for HP $C2/c$, and one for HT $C2/c$ (Downs et al. 1999). The model and the procrystal electron-density distributions produced the same arrangement of bond-critical points, demonstrating that the two distributions predict the same sets of atomic coordination. Figure 8 shows plots of $\rho(\mathbf{r}_C)$ and $\nabla^2\rho(\mathbf{r}_C)$ versus the $M2$–O bond lengths for these two pyroxenes. The correlations are similar for both sets of calculations, except that the procrystal values are larger than those obtained from the model calculations. It is surprising that the model calculation should result in less electron density at the bond-critical point than the procrystal calculation. The cause of this difference is unknown to us.

In each of the three different phases of kanoite, the electron-density distributions exhibit different bond-critical point distributions around the Mn2 site. Each have 6 bcps, with bonds indicated to exist between the Mn2 and the four O1 and O2 atoms that are shared with

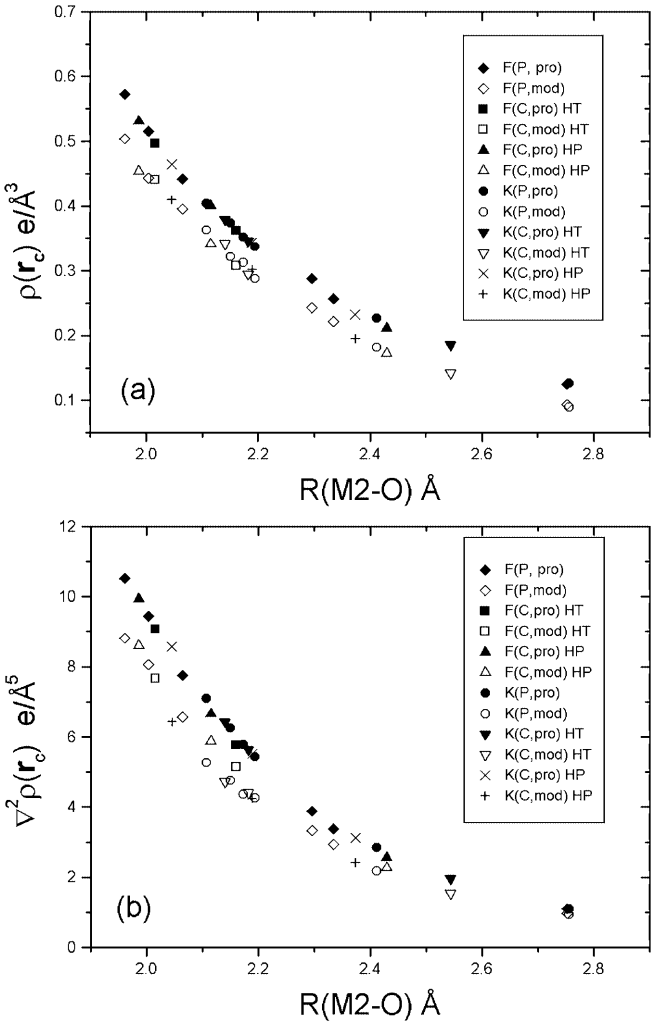

Fig. 8a, b Plots of **a** $\rho(\mathbf{r}_C)$ and **b** $\nabla^2\rho(\mathbf{r}_C)$ versus the *M*2O bond length computed with the procrystal and ab initio models for the pyroxenes kanoite ($MnMgSi_2O_6$) and ferrosilite ($Fe_2Si_2O_6$) at pressure and temperature conditions corresponding to symmetries $C2/c$ and $P2_1/c$

the octahedral chain of $M1O_6$ groups, as illustrated in Fig. 9. The structural differences between the three phases are related to the bonding between Mn2 and the bridging O3 atoms, as suggested by Sueno et al. (1984), and are readily apparent from the distribution of the bcps. Bond-critical points are found between Mn2 and $O3_2$ and $O3_4$ for the $P2_1/c$ phase, between Mn2 and $O3_1$ and $O3_4$ for the HP $C2/c$ phase, and between Mn2 and $O3_2$ and $O3_3$ for the HT $C2/c$ phases.

The distribution of the critical points around the Fe2 atom in clinoferrosilite also varies for the three phases. Bond-critical points are found between Fe2 and $O3_2$ and $O3_4$ for the $P2_1/c$ phase and between Fe2 and $O3_1$ and $O3_4$ for the HP $C2/c$ phase, but none was found between Fe2 and any bridging O3 atom for the HT $C2/c$ phases. Unlike the case for $CaSi_2O_5$, there is no evidence for ellipticity in the *M*2–O3 bonds for either pyroxene in either of the two electron-density distributions.

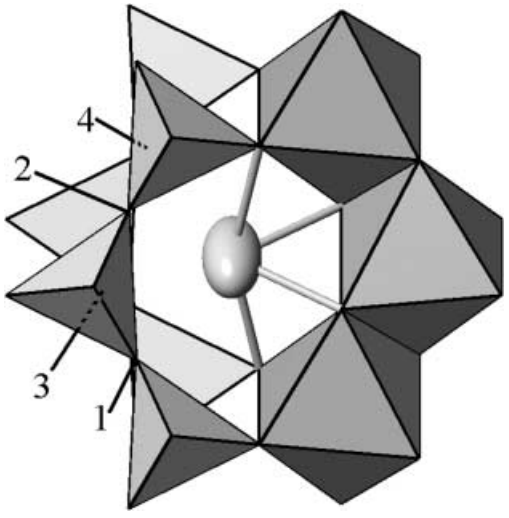

Fig. 9 A portion of the structure of a pyroxene with SiO_4 groups rendered as tetrahedra, $M1O_6$ groups as octahedra, and the *M*2 atom as a displacement ellipsoid. All O3 atoms bridge the tetrahedra, and are *labeled* to define the positions *1–4*, as used in the text. The bonds between *M*2–O1 and *M*2–O2 are indicated by *rigid rods*

Some concluding remarks

The bond-critical point properties calculated for a procrystal representation of the electron-density distribution of a crystal are highly correlated with the bcp properties calculated for the ab initio model electron-density distribution. For bonded interactions involving some of the more electropositive *M* cations, the magnitudes of the procrystal properties are in good agreement with those generated for the model distributions, particularly the values for $\rho(\mathbf{r}_C)$, $r_b(O)$, and $\nabla^2\rho(\mathbf{r}_C)$. Furthermore, regardless of the electronegativity of the *M* cation, the procrystal bonded radius of the oxide anions agrees within 0.03 Å with that determined for the model electron-density distribution. In other words, the procrystal distribution does a good job in locating the position of the bcp between a pair of atoms. Given that the promolecule distributions generated in this study of more than 300 unique oxide bonds reproduced all of the bond paths and bcp generated by the model distributions, it appears that the procrystal distribution for minerals is capable of generating (1) the bond paths between bonded atoms, (2) the coordination number of atoms, and (3) trends in the bond-critical point properties. This study also suggests that bonding is not a consequence of the migration of electrons into a bonding region, but instead, bonding is largely atomic in nature. Bonding takes place when two atoms are brought into the appropriate geometry. The migration of electrons appears to take place in order to satisfy electrostatic forces, but it is not a sufficient condition for bonding.

Furthermore, it seems likely that any property of a crystal that depends solely upon $\rho(\mathbf{r}_C)$ and its first and second derivatives can be evaluated from the procrystal distribution with reasonable accuracy. The greatest dis-

agreement between critical-point properties of the procrystal and the ab initio model is the sharpness of the curvature of the density perpendicular to the bond path. This disagreement is systematic and can be improved simply by scaling $\lambda_{1,2}^{pro}$. Thus, it appears that the critical-point properties of the procrystal can be used to predict the properties of the ab initio model. The systematic suggests a two-stage optimization routine for ab initio calculations. First, vary only the angular components of atomic wave functions, and second, add the radial component.

Acknowledgements We are grateful to the National Science Foundation for supporting this work with grants EAR-9903104 to study the compression mechanisms of upper mantle minerals and EAR-9627458 to study bonded interactions and chemical reactivity of Earth materials based on electron-density distributions. This paper was written while G.V.G. was a National Science Funded Visiting Scholar at the University of Arizona during the spring of 2001. The faculty and graduate students of the Department of Geosciences, Bob Downs, Marcus Origlieri, Marilena Stimpfl, and Richard Thompson, in particular, are thanked for making the visit by G.V.G. great fun and a productive experience.

We also acknowledge the anonymous reviewers for their detailed and constructive comments. They greatly improved the readability of the manuscript.

References

Allan DR, Angel RJ (1997) A high-pressure structural study of microcline ($KAlSi_3O_8$) to 7 GPa. Eur J Mineral 9: 263–275

Angel RJ (1997) Transformation of fivefold-coordinated silicon to octahedral silicon in calcium silicate, $CaSi_2O_5$. Am Mineral 82: 836–839

Angel RJ, Ross NL, Seifert F, Fliervoet TF (1996) Structural characterization of pentacoordinate silicon in a calcium silicate. Nature 384: 441–444

Arlt T, Armbruster T (1997) The temperature-dependent $P2_1/c$-$C2/c$ phase transition in the clinopyroxene kanoite $MnMg[Si_2O_6]$: a single-crystal X-ray and optical study. Eur J Mineral 9: 953–964

Arlt T, Angel RJ, Miletich R, Armbruster T, Peters T (1998) High-pressure $P2_1/c$-$C2/c$ phase transition in clinopyroxenes: influence of cation size and electronic structure. Am Mineral 83: 1176–1181

Bader RFW (1990) Atoms in molecules. Oxford Science Publications, Oxford, UK

Bader RFW (1998) A bond path: a universal indicator of bonded interactions. J Phys Chem 102(A): 7314–7323

Bader RFW, MacDougall PJ (1985) Toward a theory of chemical reactivity based on charge density. J Am Chem Soc 107: 6788–6795

Bader RFW, MacDougall PJ, Lau CDH (1984) Bonded and nonbonded charge concentrations and their relation to molecular geometry and reactivity. J Am Chem Soc 106: 1594–1605

Baur WH (1987) Effective ionic radii in nitrides. Crystallogr Rev 1: 59–80

Clementi E, Roetti C (1974) Atomic data and nuclear data tables, Roothaan–Hartree–Fock atomic wave functions. Academic Press, New York

Cohen RE (1994) First-principles theory of crystalline SiO_2. In: Heaney PJ, Prewitt CT, Gibbs GV (eds) Silica, Physical behavior, geochemistry and materials applications. Reviews in Mineralogy, vol 29, 369–402. Mineralogical Society of America, Washington, DC

Coppens P (1997) X-ray charge densities and chemical bonding. IUCr texts on crystallography. Oxford Science Publications, Oxford

D'Arco P, Sandrone G, Dovesi R, Orlando R, Saunders VR (1993) A quantum-mechanical study of the perovskite structure type of $MgSiO_3$. Phys Chem Miner 20: 407–414

Dovesi R, Roetti C, Freyria-Fava C, Prencipe M, Saunders VR (1991) On the elastic properties of lithium, sodium and potassium oxide. An ab initio study. J Chem Phys 156: 11–19

Dovesi R, Saunders VR, Roetti C, Causá M, Harrison NM, Orlando R, Aprá E (1996) CRYSTAL98 user's manual. University of Torino, Torino, Italy, pp 1–170

Downs JW (1991) Electrostatic properties of minerals from X-ray diffraction data: a guide for accurate atomistic models. In: Ganguly J (ed) Diffusion, atomic ordering, and mass transport. Advances in physical geochemistry, vol 8. Springer Berlin Heidelberg New York

Downs JW (1995) The electron density distribution of coesite. J Phys Chem 99: 6849–6856

Downs JW, Swope RJ (1992) The Laplacian of the electron density and the electrostatic potential of danburite, $CaB_2Si_2O_8$. J Phys Chem 96: 4834–4840

Downs RT, Hazen RM, Finger LW (1994) The high-pressure crystal chemistry of low albite and the origin of the pressure dependency of Al–Si ordering. Am Mineral 79: 1042–1052

Downs RT, Andalman A, Hudasko M (1996) The coordination number of Na and K in low albite and microcline as determined from a procrystal electron density distribution. Am Mineral 81: 1344–1349

Downs RT, Gibbs GV, Boisen MB, Jr. (1999) Topological analysis of the $P2_1/c$ to $C2/c$ transition in pyroxenes as a function of temperature and pressure. EOS Transactions, AGU, Fall Meeting Supplement 80, F1140

Feth S, Gibbs GV, Boisen MB, Jr., Myers RH (1993) Promolecule radii for nitrides, oxides and sulfides. A comparison with effective ionic and crystal radii. J Phys Chem 97: 11 445—11 450

Gatti C (1997) TOPOND96 user's manual. CNR-CSRSRC, Milano, Italy, 1–15

Gatti C, Bianchi R, Destro R, Merati F (1992) Experimental vs. theoretical topological properties of charge-density distributions – an application to the L-alanine molecule studied by X-ray diffraction at 23 K. THEOCHEM – J Mol Struct 255: 409–433

Geisinger KL, Spackman MA, Gibbs GV (1987) Exploration of structure, electron-density distribution and bonding in coesite with Fourier and pseudoatom refinement methods using single-crystal X-ray diffraction data. J Phys Chem 91: 3237–3244

Gibbs GV, Spackman MA, Boisen MB, Jr. (1992) Bonded and promolecule radii for molecules and crystals. Am Mineral 77: 741–750

Gibbs GV, Boisen MB, Jr., Beverly LL, Rosso KM (2001) A computational quantum-chemical study of the bonded interactions in Earth materials and structurally and chemically related molecules. Molecular modeling theory: applications in the geosciences. Reviews in Mineralogy and Geochemistry, vol 42, pp 345–382. Cygan RT, Kubicki JD, Rosso JJ (series ed) Mineralogical Society of America, Washington, DC

Goldsmith JR (1986) The role played by H in promoting Al–Si interdiffusion in albite ($NaAlSi_3O_8$) at high pressures. Earth Planet Sci Lett 80: 135–138

Hill RJ, Newton MD, Gibbs GV (1983) A crystal-chemical study of stishovite. J Sol State Chem 47: 185–200

Hill FC, Gibbs GV, Boisen MB (1997) Critical-point properties of electron density distributions for oxide molecules containing first- and second-row cations. Phys Chem Miner 24: 582–596

Hugh-Jones D, Woodland A, Angel R (1994) The structure of high-pressure $C2/c$ ferrosilite and crystal chemistry of high-pressure $C2/c$ pyroxenes. Am Mineral 79: 1032–1041

Ivanov YU, Belokoneva EL, Protas J, Hansen NK, Tsirelson VG (1998) Multipole analysis of the electron density in topaz using X-ray diffraction data. Acta Crystallogr (B) 54: 774–781

Kirfel A, Gibbs GV (2000) Experimental electron-density distributions and bonded interactions for fibrous zeolites natrolite, mesolite and scolecite and related materials. Phys Chem Miner 27: 270–284

Knop O, Boyd RJ, Choi SC (1988) S–S bond lengths, or can a bond length be estimated from a single parameter? J Am Chem Soc 110: 7299–7301

Kuntzinger S, Ghermani NE, Dusausoy Y, Lecomte C (1998) Distribution and topology of the electron density in an aluminosilicate compound from high-resolution X-ray diffraction data: the case of scolecite. Acta Crystallogr (B) 54: 819–833

MacDougall PJ (1989) The Laplacian of the electron charge distribution. PhD Thesis, McMaster University, Hamilton, Ontario, Canada, 128 p

Maslen EN, Etschmann BE (2000) Bonding without ionisation. Austral J Phys 53: 299–316

Pisani C (1996) Quantum mechanical ab initio calculation of the properties of crystalline materials. Springer Berlin Heidelberg New York, 328 p

Shannon RD (1976) Revised effective ionic radii and systematic studies of interatomic distances in halides and chalcogenides. Acta Crystallogr (A) 32: 751–767

Shannon RD (1981) Bond distances in sulfides and a preliminary table of sulfide crystal radii. In: O'Keeffe M, Navrotsky A (eds) Structure and bonding in crystals, vol II. Academic Press New York, NY, pp 53–70

Shannon RD, Prewitt CT (1969) Effective ionic radii in oxides and fluorides. Acta Crystallogr (B) 25: 925–946

Slater JC (1965) Quantum theory of molecules and solids. Symmetry and energy bands in crystals, vol 2. McGraw-Hill, New York

Spackman MA, Maslen EN (1985) Electron density and the chemical bond. Reappraisal of Berlin's theorem. Acta Crystallogr (A) 41: 347–353

Spackman MA, Maslen EN (1986) Chemical properties from the promolecule. J Chem Phys 90: 2020–2027

Spackman MA, Hill RJ, Gibbs GV (1987) Exploration of structure and bonding in stishovite with Fourier and pseudoatom refinement methods using single-crystal and powder X-ray diffraction data. Phys Chem Miner 14: 139–150

Stewart RF (1991) The application of charge density research in chemistry and drug design. Jeffrey GA, Piniella JF (eds) NATO-ASI Series, Plenum, New York

Sueno S, Kimata M, Prewitt CT (1984) The crystal structure of high clinoferrosilite. Am Mineral 69: 264–269

Tosi MP, Fumi FG (1964) Ionic sizes and Born repulsive parameters in the NaCl-type alkali halides – II. The generalized Huggins-Mayer form. J Phys Chem Sol 25: 45–52

Trefry MG, Maslen EN, Spackman MA (1987) Electrostatic, Madelung and cohesive energies for solids. J Phys (C) Sol State Phys 20: 19–27

Tsirelson VG, Zou PF, Tang TH, Bader RFW (1994) Topological definition of crystal structure – determination of the bonded interactions in solid molecular chlorine. Acta Crystallogr (A) 51: 143–153

Tsirelson VG, Abramov YA, Zavodnik VE, Stash AI, Belokoneva EL, Stahn J, Pietsch U, Feil D (1998a) Critical points in a crystal and procrystal. Struct Chem 9: 249–254

Tsirelson VG, Avilov AS, Abramov YA, Belokoneva EL, Kitaneh R, Feil D (1998b) X-ray and electron diffraction study of MgO. Acta Crystallogr (B) 54: 8–17

Warren MC, Redfern SAT, Angel RJ (1999) Change from sixfold to fivefold coordination of silicate polyhedra: insights from first-principles calculations of $CaSi_2O_5$. Phys Rev (B) 59: 9149–9154

Xiao Y (1998) Molecular modeling of geochemical processes: from atmospheric to water-rock interface. PhD Thesis, Yale University, New Haven, CT